

JPL D-16479

Tropospheric Emission Spectrometer (TES)
Level 1B Algorithm Theoretical Basis
Document

H. M. Worden and K. W. Bowman
Version 1.1

Approved: Reinhard Beer
Principle Investigator

Jet Propulsion Laboratory
California Institute of Technology

This document was prepared at the Jet Propulsion Laboratory, California Institute of Technology, under a contract from the National Aeronautics and Space Administration

Contents

1	Introduction	1
1.1	Purpose	1
1.2	Scope	1
1.3	Applicable Documents	2
1.3.1	Controlling Documents	2
1.3.2	Project Reference Documents	2
1.4	Revision History	2
1.5	Revision Date	2
2	Background	3
2.1	Experiment Objectives	3
2.2	Relevance to Earth System Science	4
2.3	Instrument Characteristics	4
2.4	Instrument ground and flight calibration	5
3	Algorithm Overview	8
3.1	TES Data Processing	8
3.2	Level 1B Processing Flow	9
4	Transformation of Interferograms to Spectra	14
4.1	Introduction	14
4.2	Gain and non-linearity corrections	15
4.3	Interferogram re-index	18
4.4	Prime-factor FFT	19
4.5	Spectral spike mask generation	19
5	Radiometric Calibration	21
5.1	Introduction	21

5.2	Calibration phase alignment	24
5.3	Time interpolation of calibration spectra	26
5.4	Frequency scale determination	27
5.5	Calculation of radiometrically calibrated spectra	28
5.5.1	Target spectrum phase alignment	29
5.5.2	Limb view calibration	31
5.6	NESR estimation	32
5.7	Systematic errors	33
5.8	Algorithm validation	34
6	Off-axis ILS Correction and Modeling	35
6.1	Introduction	35
6.2	Fresnel approximation	36
6.3	Validation for broad band spectra	41
6.4	Non-uniform illumination	42
7	Spectral Calibration	46
7.1	Frequency scale adjustments to match model line positions	46
7.1.1	Line selection	47
7.1.2	Determination of frequency shifts	48
7.2	Resampling to the common L2 frequency grid	52
7.3	Algorithm validation	52
8	Data Quality Assessment	54
8.1	Introduction	54
8.2	Cloud and anomaly detection	54
8.3	Undesired instrument effects	57
8.4	Processing errors and data quality history	59
Appendix A	Broad Band Off-Axis ILS Correction and Modeling	60
A.1	Filter banks	60
A.2	Off-axis ILS algorithm for the 2-channel case	65
Appendix B	Optional Phase Correction Techniques	73
B.1	Introduction	73
B.2	Optimal phase estimator	75
B.3	FVS phase estimation	76
Bibliography		79

Appendix C Instrument Description

82

Notation

$B(\nu, T)$	Planck function for frequency ν and temperature T .
$C_{bb}(\nu, T_{bb})$	complex measured spectrum for calibration blackbody view.
$C_{cs}(\nu)$	complex measured spectrum for cold space view.
$C_{target}(\nu)$	complex measured spectrum for target view (nadir or limb).
$L_{target}(\nu)$	target (nadir or limb) radiance.
$L_{cs}(\nu)$	cold space radiance.
$L_{fo}(\nu)$	foreoptics radiance.
$L_{ifmtr}(\nu)$	interferometer radiance, <i>e.g.</i> beamsplitter emission.
$L_{crp}(\nu)$	radiance from cold reference plate (180K, $\epsilon = 1$), assumed to be 180° out of phase with incoming (forward) radiance.
$I(x)$	the measured modulated intensity as a function of the interferometer optical path difference.
$I_o(x)$	the modulated intensity incident on the detector.
$r(\nu)$	instrument response function.
$\epsilon_{bb}(\nu)$	blackbody emissivity.
$\phi(\nu)$	optical and electronic instrument phase for forward radiance.
$\phi_\delta(\nu)$	phase difference for radiance from beamsplitter or other interferometer components emitting out of phase from either incoming (forward) radiance or backward (cold reference plate) radiance.
$\phi_{sampling}(\nu)$	sampling phase = $2\pi m\nu/\nu_l$ where m is an integer. Phase of 1 sample corresponds to the phase for a single laser fringe offset from ZPD (<i>i.e.</i> , $m=1$).
ν_l	laser frequency (about 9397 cm^{-1} for Nd:YAG laser).
N_{step}	number of laser fringe samples per interferogram index.
N_{alias}	alias number.

Acronyms

AES	Airborne Emission Spectrometer
ATBD	Algorithm Theoretical Basis Document
BB	Blackbody
CHEM	Chemistry Mission (EOS 3rd spacecraft)
DAAC	Distributed Active Archive Center
DN	Data Numbers
EOS	Earth Observing System
FFT	Fast Fourier Transform
FTS	Fourier Transform Spectrometer
HITRAN	High resolution transmission molecular absorption database
ILS	Instrument Line Shape
JPL	Jet Propulsion Laboratory, California Institute of Technology
LaRC	Langley Research Center
MIPAS	Michelson Interferometer for Passive Atmospheric Sounding
MTPE	Mission to Planet Earth
NASA	National Aeronautics and Space Administration
NESR	Noise equivalent spectral radiance
OPD	Optical path difference
PCS	Pointing control system
PRT	Platinum resistance thermometer
RMS	Root mean square
SCF	Science Computing Facility
SNR	Signal to noise ratio
TBD	To be determined
TBS	To be specified
TES	Tropospheric Emission Spectrometer
ZPD	Zero path difference

Chapter 1

Introduction

1.1 Purpose

This Algorithm Theoretical Basis Document (ATBD) describes the algorithms used to produce Tropospheric Emission Spectrometer (TES) radiometrically calibrated spectra. These spectra are the input measurements to the Level 2 retrieval algorithm that will produce the TES Standard Data Products scheduled to be processed and archived at the NASA Langley Research Center (LaRC) Distributed Active Archive Center (DAAC).

This document identifies: sources of input data that are required for the Level 1B corrections and calibrations; provides the physical theory and mathematical background underlying the use of this information; describes practical considerations affecting algorithm development; and outlines a test and validation approach.

1.2 Scope

This document covers the algorithm theoretical basis for the calibration strategy and correction parameters to be included in the TES Level 1B processing at or near launch time. On-going development and prototyping efforts may result in modifications to parts of certain algorithms. Only the algorithms which are implemented at the DAAC for routine processing of TES data will be preserved in the final release of this document.

1.3 Applicable Documents

1.3.1 Controlling Documents

Mission to Planet Earth Strategic Enterprise Plan 1998-2002. NASA HQ MTPE, October 1998

Execution Phase Project Plan for the Earth Observing System (EOS). GSFC 170-01-01, Rev. A, May 1995

1.3.2 Project Reference Documents

Tropospheric Emission Spectrometer: Scientific Objectives & Approach, Goals & Requirements JPL D-11294, Rev. 6.0, April 1999

1.4 Revision History

Version 1.0 of this document is dated January 15, 1999

1.5 Revision Date

The document was last revised on October 29, 1999.

Chapter 2

Background

2.1 Experiment Objectives

The Tropospheric Emission Spectrometer (TES), selected for flight on the EOS CHEM-1 mission, will provide the first global view of the chemical state of the troposphere (the lowest region of the atmosphere, extending from the surface to about 10-15 km altitude). The investigation will focus on mapping the global distribution of tropospheric ozone and on understanding the factors that control ozone concentrations.

Ozone is produced in the troposphere by photochemical oxidation of carbon monoxide (CO) and hydrocarbons in the presence of nitrogen oxides (NO_x) and water vapor. These ozone precursors have both natural and anthropogenic sources. The chemistry of ozone is complex and tightly coupled to the atmospheric transport of both ozone and the precursors.

Tropospheric ozone has three major environmental impacts:

AS AN AIR POLLUTANT. Ozone in surface air is toxic to humans, animals and vegetation. It is the principal harmful component of smog.

AS A CLEANSING AGENT. Photolysis of ozone in the presence of water vapor is the primary source of the hydroxyl radical (OH), which is the main oxidant in the atmosphere. Reactions with OH in the lower and middle troposphere are the principal sink for a large number of environmentally-important species including air pollutants (carbon monoxide), greenhouse gases (methane), and gases depleting the stratospheric ozone layer (HCFC's, methyl halides).

AS A GREENHOUSE GAS. Ozone in the middle and upper troposphere is an efficient greenhouse gas. Perturbation of ozone in this region of the atmosphere

results in heterogeneous radiative forcing with complicated implications for climate.

The troposphere contains only about 10% of the total ozone in the atmosphere - the bulk is in the stratosphere. The environmental implications of tropospheric ozone are very different from those of stratospheric ozone. The ozone layer in the stratosphere shields the Earth's surface from solar UV-B radiation, and thinning of this layer as a result of human activities is a matter of grave concern. Tropospheric ozone, by contrast, has increased as a consequence of human activity (primarily because of combustion processes). Whether this increase in tropospheric ozone is beneficial (cleansing agent) or harmful (air pollutant, greenhouse gas) depends to a large extent on its altitude. It is very important, therefore, to map the global 3-dimensional distribution of tropospheric ozone and its precursors in order to improve our understanding of the factors controlling ozone in different regions of the troposphere.

The specific Standard Products that TES will produce are global-scale vertical concentration profiles (0 to ≈ 33 km) of ozone, water vapor, carbon monoxide, methane, nitric oxide, nitrogen dioxide and nitric acid (the latter 3 in the mid- and upper troposphere only). Essential by-products of the analysis are atmospheric temperature profiles and surface temperature and emissivity.

2.2 Relevance to Earth System Science

One of the primary EOS themes is "Atmospheric Ozone Research". TES directly addresses this theme.

2.3 Instrument Characteristics

TES is an infrared, high resolution, Fourier Transform spectrometer (FTS) covering the spectral range $650 - 3050 \text{ cm}^{-1}$ ($3.3 - 15.4 \mu\text{m}$) at a spectral resolution of 0.1 cm^{-1} (nadir viewing) or 0.025 cm^{-1} (limb viewing). The two observation modes are essential because many of the spectral features that TES observes are very weak (especially the nitrogen oxides) and limb-viewing markedly enhances their measurability (with the deficiency that cloud interference is much more likely than in nadir viewing).

In order to improve signal-to-noise ratio and improve collection efficiency, TES is (as far as possible) radiatively-cooled to 180K and divides the spectral

range into 4 sub-regions each observed with a separate 1x16 array of detectors actively cooled to 65K. The bandwidth is further restricted to about 250 cm^{-1} by interchangeable filters. Table (2.1) lists the frequency ranges and sampling information¹ for the TES filter bands. With the TES detector arrays, 16 altitudes in the troposphere and lower stratosphere are observed simultaneously with a height separation of 2.3 km or, alternatively, 16 contiguous areas, each 0.5 x 5 km, are observed on the ground.

It is a property of a Fourier Transform Spectrometer that it must be used in a so-called "staring" mode (that is, the target location or altitude must be tracked). Accordingly, TES is equipped with a precision pointing system.

The current TES mission plan is to collect data in a "Global Survey" mode in cycles of 4 days on, 4 days off, where the "off" days may be used for other types of measurements. The Global Survey data are used to generate the TES standard products. In the Global Survey mode, TES obtains its data in 4 seconds (nadir) or 16 seconds (limb) plus calibrations in a sequence: 2 calibrations followed by 2 nadir observations followed by 3 limb observations (see Table (2.2)). The entire sequence requires 81.2 seconds and is repeated continuously for 58 orbits. Each 4-day (58 orbit) Global Survey is preceded and followed by calibration-only sequences. TES also has unique capabilities for targets-of-opportunity such as volcanic eruptions, biomass burning regions or regional ozone episodes, which can be targeted specifically during the "off" days. A more detailed description of the instrument can be found in [Beer *et al.*, 1999]. A copy of this paper has been appended to the end of this ATBD.

2.4 Instrument ground and flight calibration

The characterization and calibration of the hardware begins with a preflight calibration of the radiometric, spatial, and spectral response of the instrument. These measurements are used to calibrate and characterize the performance of the instrument, establish a calibration baseline, provide input into development of the system radiometric model, and define the input corrections to the Level-1A and -1B algorithms.

Following launch, the instrument's Onboard Calibration Subsystem is used to calibrate the in-flight radiometric and spatial response of the instrument. The in-flight spectral calibration is derived from measured spectra of the atmosphere.

¹A complete discussion of FTS sampling and alias effects can be found in [Beer, 1992].

Table 2.1: TES optical filter band and sampling information

Filter ID	Filter Half-Power Pts (cm^{-1})		Sampling Step	Alias Number	Alias Boundaries (cm^{-1})		Number Nadir Ifgm Pts*
1A1	1900	2250	8	4	1761	2348	19836
1A2	2200	2450	9	5	2087	2609	17632
1A3	2425	2650	12	7	2348	2740	13224
1A4	2600	2850	8	5	2348	2935	19836
1A5	2800	3050	9	6	2609	3131	17632
1B1	820	1050	8	2	587	1174	19836
1B2	950	1150	11	3	854	1281	14426
2A1	1100	1325	10	3	939	1409	15869
2A2	1300	1550	8	3	1174	1761	19836
2A3	1500	1750	10	4	1409	1879	15869
2A4	1700	1950	9	4	1566	2087	17632
2B1	650	900	9	2	522	1044	17632

*The numbers of points for limb interferograms are 4 X the numbers for the nadir interferograms.

Table 2.2: Proposed TES Global Survey Data Sequence

Scan Number	Viewing Mode	Scan Time* (seconds)	Filters [†]			
1	cold space cal.	4	1A1	1B1	2A2	2B1
2	blackbody cal.	4	1A1	1B1	2A2	2B1
3	nadir 1	4	1A1	1B2	2A2	2B1
4	nadir 2	4	1A1	1B2	2A2	2B1
5	limb 1	16	1A1	1B1	2A2	2B1
6	limb 2	16	1A1	1B2	2A4	2B1
7	limb 3	16	1A1	1B2	2A4	2B1

*Time including resets and turnaround is 81.2 seconds per sequence.

[†]Calibrations of filters 1B2 and 2A4 are performed in subsequent sequences. See Table XXVI in [Beer, 1999].

Additional in-flight calibration activities are planned for monitoring nonlinearities in the instrument's output, changes in the signal-chain gain calibration, and the calibration stability between the high- and low-resolution modes.

The radiometric, spatial, and spectral calibrations of the instrument are established and maintained from the following measurements:

1. The preflight radiometric calibration uses measurements taken while viewing two high-emissivity blackbody cavities. The radiometric calibration is maintained on orbit from measurements taken while viewing the instrument's internal, National Institute of Standards and Technology (NIST)-traceable radiometric source.
2. The preflight spatial calibration is provided by measurements taken as a sub-pixel-sized image of an infrared illuminated slit is scanned across each detector. These measurements, along with the calibrated spatial response of each pixel (as provided by the Focal Plane Subsystem), provide the information required to spatially characterize the instrument. An identical method is used on orbit to monitor the spatial properties of the instrument. The onboard spatial calibration source provides the IR image of a slit moved across the detector by scanning the gimbal mirror across the field of view of the instrument. The measured signal from each pixel is recorded simultaneously in each of the four focal planes as a function of gimbal mirror position. These measurements map the relative positions of each pixel within the field of view of the instrument.
3. The spectral calibration of the instrument and measurement of the instrument line shape are provided by viewing a large-area blackbody source through a gas cell filled with reference test gases. The instrument records a spectrum of the gas and compares it with the known line widths of the reference test gases. The in-flight spectral calibrations are provided by comparing a measured atmospheric spectrum to well-known spectral features in the atmosphere.

A more detailed description of the instrument calibration plan can be found in [Holm, 1999].

Chapter 3

Algorithm Overview

3.1 TES Data Processing

TES data processing is divided into the following algorithmic steps: Level 1A, Level 1B, Level 2 and Level 3. The TES Level 1A software generates geolocated interferograms from Level 0 data packets. Level 1B produces calibrated science spectra. Level 2 models and inverts the spectral data to produce atmospheric temperatures and chemical composition as a function of altitude or pressure. Finally, Level 3 produces global maps of the atmospheric state parameters retrieved by Level 2. Level 1A is a reversible process, i.e. the Level 0 data packets can be produced from the geolocated interferograms. Level 1B, Level 2 and Level 3, however, are not reversible. Therefore, the Level 1A output must be archived.

TES will produce a data stream consisting of science data (limb and nadir views), calibration data (blackbody and cold space views) and ancillary information. The science and calibration data are in the form of interferograms, which are measurements of the relative intensity of light from two interfering beams as a function of optical path difference. The Fourier transforms of these interferograms are directly related to the spectra of the emitting sources [Beer, 1992]. We must perform a radiometric calibration so that the amplitudes of science spectra are in radiance units. This is done with calibration sources of known spectral radiance. Once the limb and nadir spectra are in radiance units, they can be compared to simulated spectra, which are generated by a radiative transfer model of the atmosphere. An iterative fit of this model spectra to the measured spectrum produces parameters specifying the atmospheric state.

3.2 Level 1B Processing Flow

The basic purpose of the Level 1B algorithm is to determine spectra of radiation emitted by the atmosphere from interferograms generated by the TES Fourier transform spectrometer (FTS). This calculation consists of the following steps:

1. transformation of interferograms into spectra
2. radiometric calibration
3. off-axis ILS correction
4. spectral calibration
5. data quality assessment.

Each step is denoted by a block in Figure (3.1). The first block, which is the subject of Chapter (4) starts with an interferogram; an example is shown in Figure (3.2)(a). Each point along the abscissa of the interferogram corresponds to the optical path difference of two interfering beams of radiation. The detectors in TES are designed so that there is a linear relationship between the amplitudes of the interferogram and the intensity of radiation incident on the detector pixel. Any nonlinearities in the detection process must be corrected, which is described in Section (4.2). The spectrum of the interferogram, which is shown in Figure (3.2)(b), is calculated by a fast Fourier transform (FFT). This spectrum is the product of the optical band-pass filter with the input spectrum and is off-set by the self-emission of the FTS.

After the calibration and science interferograms have been transformed into spectra, they undergo different processing steps. In particular, the calibration spectra are stored in tables as shown in the second major block of Figure (3.1). Since all calibration scans will be measured at the nadir resolution, they must be interpolated to the limb resolution.

The multiplicative and additive effects of the FTS on the spectrum are removed by radiometric calibration, which is the second block in Figure (3.1). In TES, the radiometric calibration step uses spectral sources of known radiance (on-board blackbody and cold space) to calculate the multiplicative (slope) and additive (offset) terms. This calibration, however, is complicated by two instrumental effects. The first is dispersion introduced by the FTS. This dispersion, along with not sampling the point of zero path difference, produces an asymmetric interferogram and thus a complex spectrum. These effects can be removed by the technique of phase

alignment followed by complex radiometric calibration, which are described in Section (5.5.1). The second effect comes from the fact that the sources are not measured at the same time as the science spectra. Periodic heating of the FTS by the sun, for example, will change the off-set. As long as these changes vary slowly with time, the slope and off-set terms may be interpolated to the time when the science spectra were measured. A radiometrically calibrated spectrum is shown in Figure (3.2)(c). There are some additional processing steps, however, that must be performed before the spectra can be considered calibrated.

TES measures the spectra at different spatial points with a 1x16 detector bisected by the optical axis. For these off-axis detectors, there is no longer a simple, linear relationship between the distance traversed by one arm of the interferometer and the optical path of the incident radiation. Spectra measured by these detectors are characterized by self-apodization, frequency scaling, line broadening and asymmetry. The first three effects can be corrected using a formalism discussed in Chapter (6). The last effect is modeled in Level 2. These corrections follow the radiometric calibration as shown in Figure (3.1).

The positions of spectral lines measured by TES in the limb-viewing mode are Doppler shifted. In addition, uncertainties in the metrology system and instrument geometry can lead to slight frequency dilations. These effects are removed in the spectral calibration step, which is described in Chapter (7).

The last step in the Level 1B processing is data quality assessment. The data are checked and flagged for corruption due to the instrument and/or processing. In addition, the detection of a cloudy scene—where special processing would be required for the retrieval of the atmospheric state—generates a quality flag for Level 2.

This ATBD will discuss the algorithmic issues and trade-offs involved in all of the steps needed to correct and calibrate the spectra. Any systematic errors resulting from approximations in level 1B processing must be much lower than the science requirement of a 1% radiometric accuracy. Therefore, we have arbitrarily chosen 0.1% as the maximum tolerable error in radiance that could be introduced by any of the algorithmic steps in level 1B. Because of the complexity of the calibration and correction process, algorithm validation will be described for each step. Some of the research necessary to determine optimal techniques is on-going. Therefore, the current best strategies will be presented in each revision. Furthermore, the Level 1B algorithms will evolve to account for new information from TES pre-flight characterization and from TES on-orbit once those data are available. This ATBD does not cover the validation and calibration plan for the hardware. This plan is described in [Holm, 1999].

Many examples provided in this document use data from the Airborne Emission Spectrometer (AES). AES, a prototype instrument for TES, is also an infrared Fourier transform spectrometer and was designed for remote sensing of the troposphere from an airborne platform. AES has collected several data sets such as ocean, cloud, volcano and forest fire scenes [Worden *et al.*, 1997]. Although AES data has some features in common with TES data, and is very useful for testing the TES data processing algorithms, there are significant differences, such as the absence of a limb view on AES.

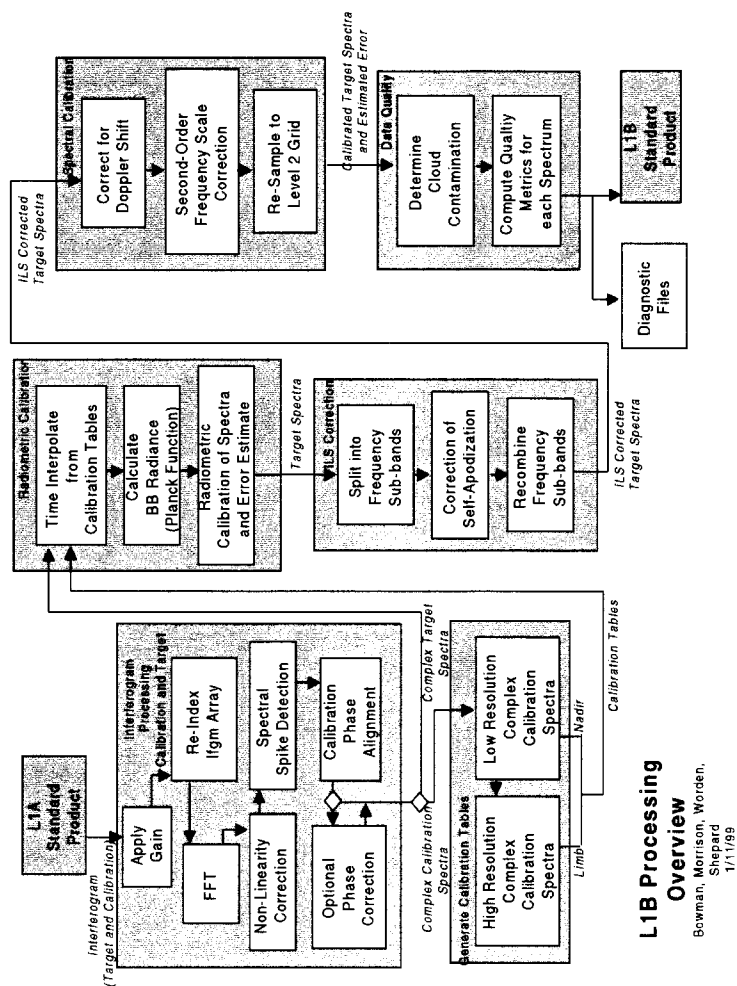


Figure 3.1: Level 1B Overview

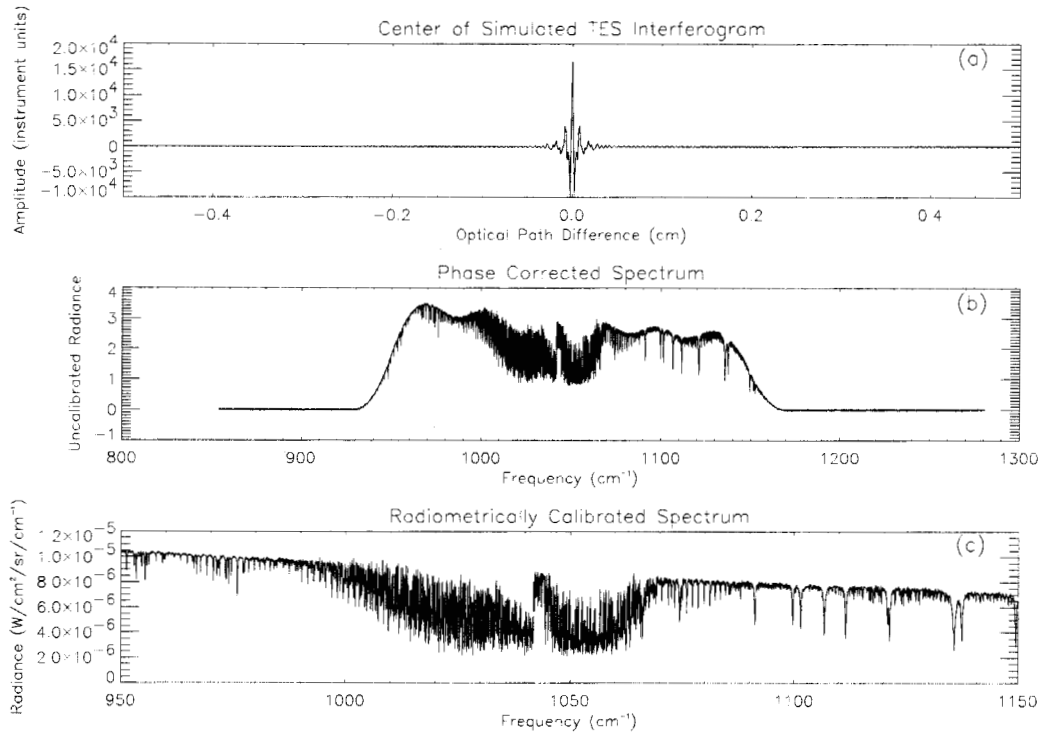


Figure 3.2: (a) Simulated TES nadir view interferogram. This figure shows only the center of the interferogram; the full interferograms extend to ± 8.45 cm and ± 33.8 for nadir and limb views respectively. (b) Uncalibrated spectrum after phase correction. Note that the dominant feature is the shape of the optical filter, which is removed by the radiometric calibration. (c) Radiometrically calibrated spectrum. The regions with higher radiance values correspond to the smooth ground radiance with minimal atmospheric absorption. The strongest absorption features (*i.e.*, spectral “lines”) are due to ozone; CO₂, H₂O and N₂O features are also present.

Chapter 4

Transformation of Interferograms to Spectra

4.1 Introduction

The measured output of an FTS is an interferogram, which records the intensity of interference between two beams of radiation as a function of optical path difference. An example of an interferogram is shown in Figure (3.2)(a). For an ideal FTS, the maximum is always at the center and the interferogram is always symmetric. In fact, the interferogram may also be thought of as an autocorrelation function [Goodman, 1985] of the source. The spectral radiance of the radiation can be related to the autocorrelation through the following Fourier transform relationship¹:

$$I(x) = \int_{-\infty}^{\infty} L(\nu) e^{i2\pi\nu x} d\nu, \quad (4.1)$$

where I is the interferogram, x is the optical path difference, L is the spectral radiance, and ν is frequency in cm^{-1} . Thus, the interferogram and the spectrum are Fourier transform pairs, which is denoted as

$$I(x) \xleftrightarrow{\mathcal{F}} L(\nu). \quad (4.2)$$

Equations (4.1) and (4.2) are the heart of an FTS.

¹Since TES is an AC coupled system, the DC component of the interferogram is effectively removed.

There are several factors that complicate this basic transform relationship. Compare the ideal interferogram in Figure (3.2) to the real AES interferogram shown in Figure (4.1), with the resulting real and imaginary spectral terms of the FFT shown in Figure (4.2). The interferogram is sampled at discrete points. The zero path difference (ZPD) of the interferogram, which is the peak in Figure (3.2)(a), is not sampled. This effectively shifts the interferogram $I(x + \delta x)$ and adds a linear phase to the spectrum $L(v) \exp(2\pi i \delta x v)$. In addition, there are dispersive elements in the optical and electrical system that change the optical path difference of the incoming radiation as a function of wavelength. This dispersion adds a non-linear phase function to the spectrum. The results of these phase terms are asymmetry in interferogram space, as seen in Figure (4.1), and a complex spectrum, which is shown in Figure (4.2). The phase of the spectrum is related to its complex components by

$$\phi(v) = \arctan \left(\frac{\text{Im}(L(v))}{\text{Re}(L(v))} \right). \quad (4.3)$$

A typical phase function is shown in Figure (5.2). The algorithms for removing these phase terms during calibration are discussed in Section (5.5.1).

4.2 Gain and non-linearity corrections

The detectors in TES are designed so that there is a linear relationship between the amplitudes of the interferogram and the modulated intensity of radiation incident on the detector pixel. Nevertheless, there may be small non-linearities present. We model the relationship between the input radiance and the output of the detector as an N -order polynomial

$$I(x) = \sum_{n=0}^M \alpha_n (I_o(x))^n, \quad (4.4)$$

where x is the optical path difference, M is the maximum order of the polynomial, I is the data number from the output of the detectors and I_o is the intensity of the input radiance. First, we correct for the variable signal chain gain, which is α_1 in Equation (4.4). A variable signal chain gain allows us to optimize the dynamic range for different types of source signal levels (such as the hot calibration black-body compared to cold space). This signal chain correction must be done in order to perform a radiometric calibration since the instrument data numbers (DN) must be on the same amplitude scale for all measurements.

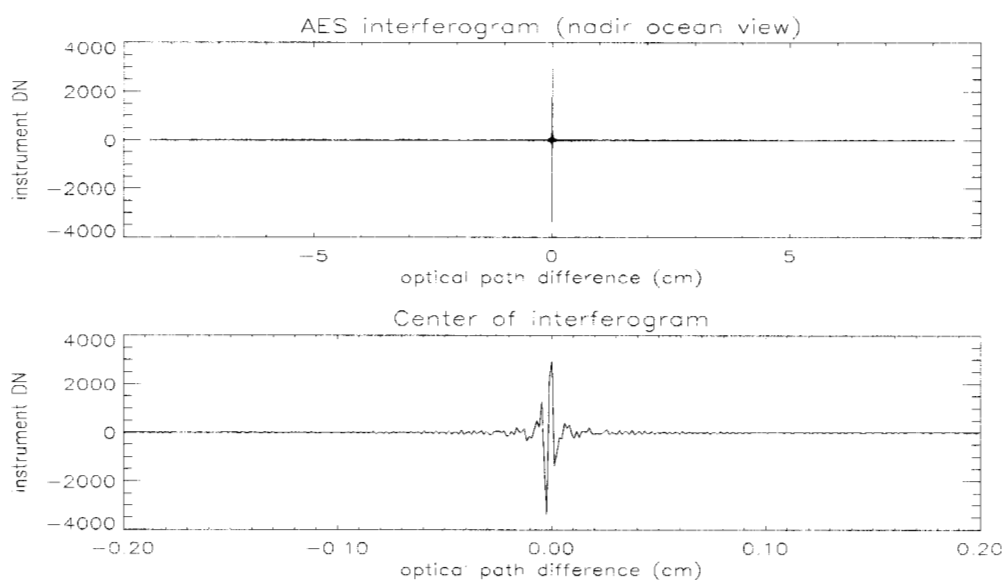


Figure 4.1: AES interferogram of a nadir ocean view using the optical filter band from 950 to 1150 cm^{-1} . The bottom panel shows a close-up of the center of the interferogram, or “kernel”. TES interferograms are also double-sided and subject to the same types of sampling and phase errors that result in the asymmetry seen in this AES interferogram.

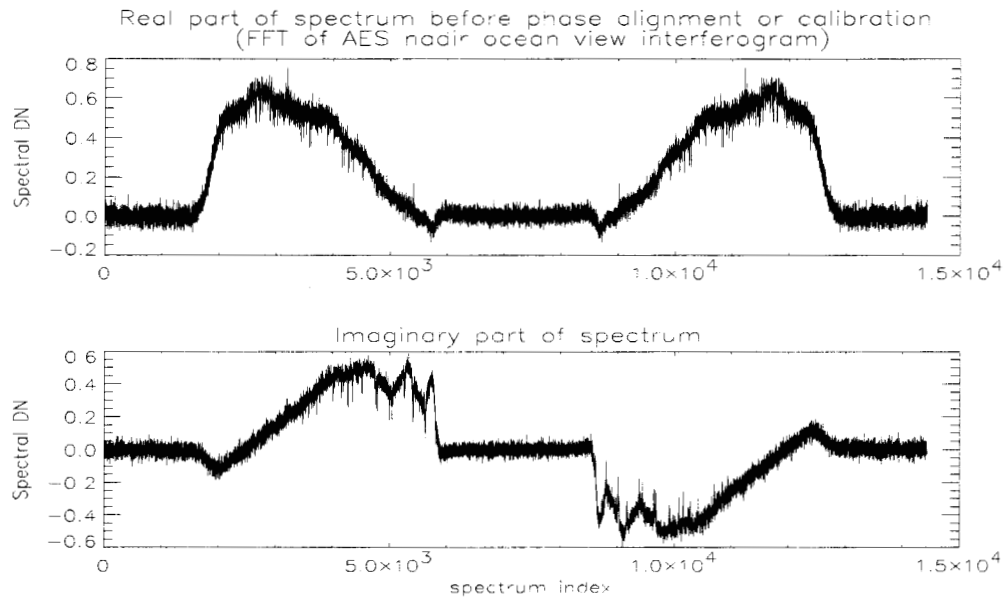


Figure 4.2: The real and imaginary spectral parts of the FFT of Figure (4.1) (after shifting the interferogram maximum to zero index). Since the measured interferogram is purely real, the resulting FFT is Hermitian, *i.e.*, the real part is symmetric and the imaginary part is anti-symmetric. Both real and imaginary have signal inside the spectral indices corresponding to the optical filter frequencies and only noise outside. After this step, only half of the mirror images are retained, the left side for spectra sampled in an odd alias and the right side for spectra with even alias numbers. (Alias numbers are listed in Table (2.1).)

Ideally, $I(x)$ is proportional to I_o , i.e., $\alpha_n = 0$ for $n \neq 1$. We expect the system response to be linear since we are using PV MCT detectors. However, if there are nonlinearities in the detectors or electronics then some form of Equation (4.4) must be used.

The linearity of the detectors will be measured on the ground and after launch by looking at the noise outside of the optical filter band-pass for each detector. The mean of the noise in this region should be close to zero, otherwise a non-linearity correction will be needed. The non-linearity of the signal chain will be tested by measuring known intensities from a blackbody at several temperatures and then fitting the amplitude of the data numbers to a polynomial. The polynomial coefficients derived from this fit are then used to solve Equation (4.4) for the intensity of the input radiance.

4.3 Interferogram re-index

Before a Fourier transform is performed on the interferogram arrays, they must be truncated or zero-padded so that the number of points on either side of the optical zero path difference (ZPD) is close to symmetric and the total number of points is set to a number that is efficient for performing the prime-factor FFT (see Section (4.4)). Although the actual ZPD point is not always sampled, we can find the point closest to ZPD. For nadir and blackbody calibration interferograms, this can be done by locating the maximum value of the interferogram. For limb and cold space interferograms, the closest-to-ZPD point will be found by maximizing the interferogram symmetry. The position of this closest point with respect to the center of the array should be fairly stable, and will depend on the scan direction. We will start out by performing only minimal truncation of the interferogram array sizes, which are shown in Table (2.1), so that the pre-determined FFT array sizes are numbers with small prime-factors. However, these FFT array sizes will most likely be updated once we have adequate statistics for the closest-to-ZPD points of actual TES interferograms. If some interferograms have a ZPD index that varies too much from the mean, we may need to perform zero padding instead of truncation so that the interferogram transform array sizes can be fixed for operational processing.

Once the interferogram array size is set at the pre-determined FFT length, we must shift the interferogram point closest to ZPD to zero index in order to adjust the spectral phase to something close to the smallest sampling phase.

4.4 Prime-factor FFT

An interferogram, an example of which is shown in Figure (3.2)(a), must be numerically transformed into a spectrum. This transformation is done using a Fast Fourier Transform (FFT). The most common FFT is called a dyadic or radix-2 FFT, which refers to an FFT that operates on arrays whose lengths are powers of 2. For TES, the array sizes are not dyadic and hence must be zero-padded to a dyadic length. When this zero padding is performed, however, there is a correlation, $\rho_{i,j}$, between spectral points that is given by

$$\rho_{i,j} = \text{sinc} \left(\pi |j - i| \frac{N}{N + M} \right), \quad (4.5)$$

where i and j are any two spectral indices, N is the number of points in the spectrum before zero-padding and $N + M$ is the number of points after zero-padding. Introducing correlation between spectral points complicates the retrieval algorithm and increases the computational burden in Level 2. Thus, prime-factor and mixed-radix FFT's [Oppenheim and Schaffer, 1989; Loan, 1992] are used to avoid spectral correlation. An interferogram array is truncated to an array size that has small prime-factors. The array size will be chosen beforehand for each filter and viewing condition. The prime-factor algorithm that we have tentatively chosen is the FFTW, which is one of the most efficient FFT algorithms available [Frigo and Johnson, 1998].

4.5 Spectral spike mask generation

Defects in the detectors or electronics may lead to narrow spikes in the measured spectrum, such as those shown in Figure (5.4). These spikes can corrupt the calibration and target phase alignment as well as disrupt the retrievals in Level 2. A spectral mask must be computed that de-weights these spikes for purposes of phase alignment and retrieval.

Spectral spikes are typically fixed in frequency and do not change in time. These spikes can be removed from the spectrum by first smoothing the hot calibration spectrum

$$\hat{C}_{bb}(v, 340K) = H(v) * C_{bb}(v, 340K), \quad (4.6)$$

where $*$ denotes a convolution, $H(v)$ is the frequency response of a low-pass

filter, e.g. a moving average. Since the hot calibration spectrum is smooth, Equation (4.6) will remove the spikes. The spectral mask is then defined by

$$M_{spike}(\nu) = \begin{cases} 0 & |\hat{C}_{bb}(\nu, 340K) - C_{bb}(\nu, 340K)| > \text{threshold} \\ 1 & \text{otherwise.} \end{cases} \quad (4.7)$$

Thus, if the absolute difference between the hot blackbody and its smoothed version exceed some threshold, then a spike has been detected. The spectral mask indicates which frequencies should not be used in the calibration and target phase alignment algorithms. Note that this algorithm does not *remove* the spikes from the spectra—it only produces a weighting function for the calibration and Level 2 retrieval algorithms. The actual threshold value will be determined during the commissioning phase of the instrument in space.

Chapter 5

Radiometric Calibration

5.1 Introduction

TES radiometric calibrations are performed in order to convert instrument data numbers (DN) to physical radiance units. This is done by making calibration measurements of known radiance sources, such as the on-board blackbody. For a perfect blackbody at temperature T , the radiance is given by the Planck function:

$$B(\nu, T) = \frac{2hc^2\nu^3}{\exp(\frac{h\nu}{kT}) - 1}, \quad (5.1)$$

where ν is the frequency in cm^{-1} , T is the temperature in Kelvin, h is the Planck constant, c is the speed of light and k is the Boltzmann constant. This gives the radiance $B(\nu, T)$ in $\text{W}/\text{cm}^2/\text{sr}/\text{cm}^{-1}$. For a real calibration blackbody, we must account for the emissivity, $\epsilon_{BB}(\nu)$, which is close to, but not exactly 1.0. The calibration blackbody radiance is then

$$L_{BB}(\nu, T) = \epsilon_{BB}(\nu)B(\nu, T), \quad (5.2)$$

where $B(\nu, T)$ is the Planck function, Equation (5.1). Assuming that we have already corrected any instrument non-linearities in the interferogram, we should have a linear relationship between the radiance of a measured scene and the resulting spectral DN. Figure (5.1) shows this relationship for a single frequency. Since the calibration measurements span the expected radiance levels of our science targets, we avoid inaccuracies due to extrapolation. Also note that the cold space view is a direct measurement of the TES instrument offset since the radiance from cold space alone is negligible compared to the instrument at its ambient temperatures.

If we could assume that the calibration and science spectra had no phase errors, then the response function $r(\nu)$ and the instrument offset radiance would be the slope and offset (respectively) given in Figure (5.1). We could then write the contributions to a TES measured spectrum as

$$S(\nu) = r(\nu)(L(\nu) + \text{offset}), \quad (5.3)$$

where $L(\nu)$ is the scene radiance being measured and $S(\nu)$ is the real part of the complex measured spectrum. However, we will have phase errors and we must therefore account for all contributions to our measurement, with possible phase differences. The TES complex measured spectrum, $C(\nu)$, for either a target or calibration radiance, $(L(\nu))$, can be written as

$$C(\nu) = r(\nu) \left(L(\nu) + L_{fo}(\nu) - L_{crp}(\nu) + L_{ifmtr}(\nu)e^{i\phi_\delta(\nu)} \right) e^{i\phi(\nu)} e^{i2\pi m\nu/\nu_l}, \quad (5.4)$$

where $C(\nu)$ is the measured complex spectrum, $r(\nu)$ is the instrument response function, $L_{fo}(\nu)$ is the foreoptics radiance, $L_{crp}(\nu)$ is the cold reference plate radiance, $L_{ifmtr}(\nu)$ is the interferometer radiance (*e.g.* beamsplitter emission), $\phi_\delta(\nu)$ is the phase difference between the interferometer radiance and either the input or cold reference plate ports, $\phi(\nu)$ is the optical and electronic instrument phase for the input radiance direction and $2\pi m\nu/\nu_l$ is the sampling phase where m is an integer.

Although $L(\nu)$ and the sampling phase will be different from one scan to the next for TES, the other terms should either be constant or have some slow time dependence. Therefore, if we can adjust the sampling phase so that m is the same for all of the scans, we can solve for $L(\nu)$ using the equations in Section (5.5).

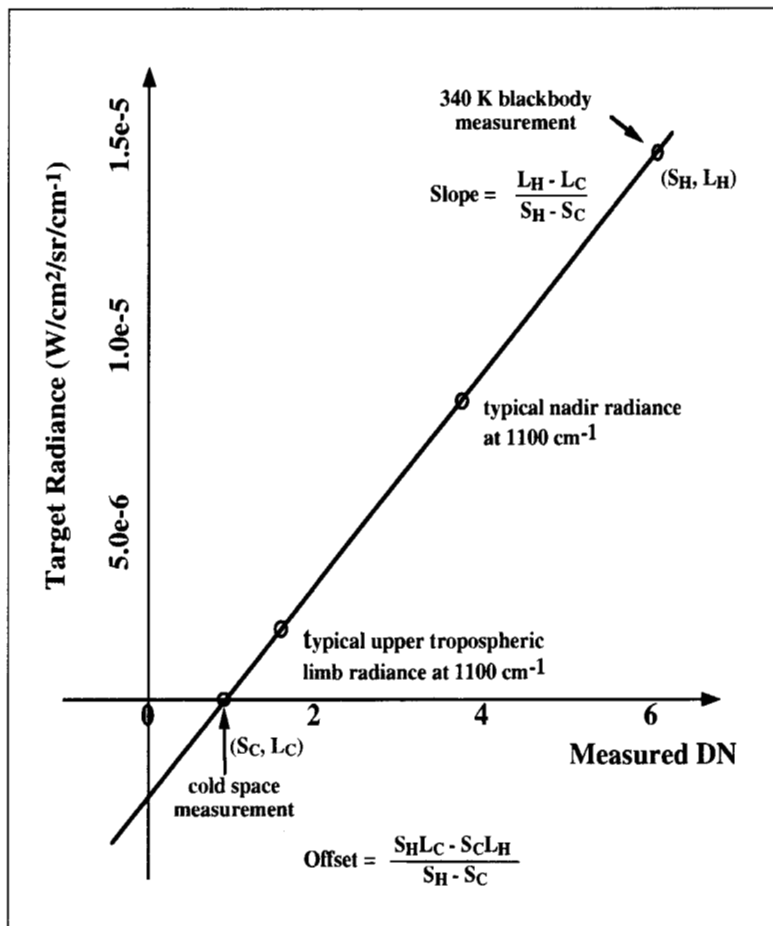


Figure 5.1: Relative radiance values for different target and calibration views at a single frequency, with arbitrary spectra instrument data numbers (DN). This assumes that phase errors in the measured spectra have been removed. S_H and S_C are the measured values (real part of complex spectra) in instrument data numbers (DN) for the blackbody and cold space calibration views respectively. L_H and L_C are the radiance values calculated from Equation (5.2) for the known calibration temperatures and emissivities. For the cold space view, we can assume $L_C = 0$, but if some other blackbody temperature is used for calibration, then this is no longer true.

5.2 Calibration phase alignment

The first step in correcting the phase of the target spectrum is to align the phase of the hot blackbody and cold space spectra, i.e., the phase of the calibration spectra is the same. The alignment of the phase is performed over a series of scans, which is called a run. When properly aligned these scans can be averaged together, which improves the signal-to-noise ratio of the spectrum and hence the calibration of the target spectrum. Calibration phase alignment consists of two steps, which are applied separately to the blackbody and cold spectra spectra. The first step takes the first scan of a run and minimizes

$$\chi(k) = \|M_{spike}(v) \text{Im}(C_{bb}(v) e^{-i2\pi kv/v_l})\|^2, \quad (5.5)$$

where $\|\cdot\|^2$ refers to the squared norm, which is chosen to be the sum-of-squares, and M_{spike} is the spectral spike mask defined in Equation (4.7). Assuming that the linear term is the dominant term in the phase function of $C_{bb}(v)$, then from Equation (5.4), $\chi(k)$ is minimal when $k = m$. Thus, Equation (5.5) insures that the phase of the first scan has been rotated close to the ZPD, i.e. where the phase function is close to zero.

This scan is now the reference scan, $C_{bb,ref}(v)$. The second step consists of aligning the other blackbody scans to the reference scan by minimizing the following equation:

$$\chi_{bb}(k) = \|M_{spike}(v) (C_{bb,ref}(v) - C_{bb,scan}(v) e^{-i2\pi kv/v_l})\|^2, \quad (5.6)$$

where $C_{bb,scan}(v)$ refers to a scan of the blackbody in a run. Assuming that the radiance terms in Equation (5.4) are fixed, then according to Equation (5.4) $\chi_{bb}(k)$ is zero when $m = k$. Thus, $C_{bb,ref}(v) = C_{bb,scan}(v) \exp\{-i2\pi mv/v_l\}$ and therefore the phase of the blackbody scan is aligned to the phase of the reference blackbody. Furthermore, the phase significantly changes for each change in m . Thus the algorithm is robust for low SNR signals such as the cold space spectra. Equation (5.6) is minimized for every scan in a run, which results in a phase-aligned run of blackbody spectra, which typically consists of 50 scans, that can be then averaged and subsequently used to calibrate the target spectra. An example with Airborne Emission Spectrometer (AES) of aligning a 340 K blackbody spectrum using Equation (5.6) is shown in Figures (5.2) and (5.3).

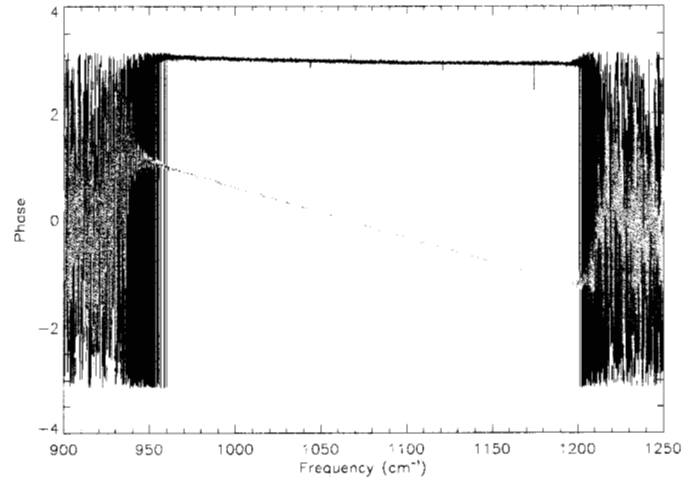


Figure 5.2: Calibration phase misalignment of an AES 340 K blackbody. The reference blackbody phase is shown in black. The original phase of a blackbody scan is shown in green.

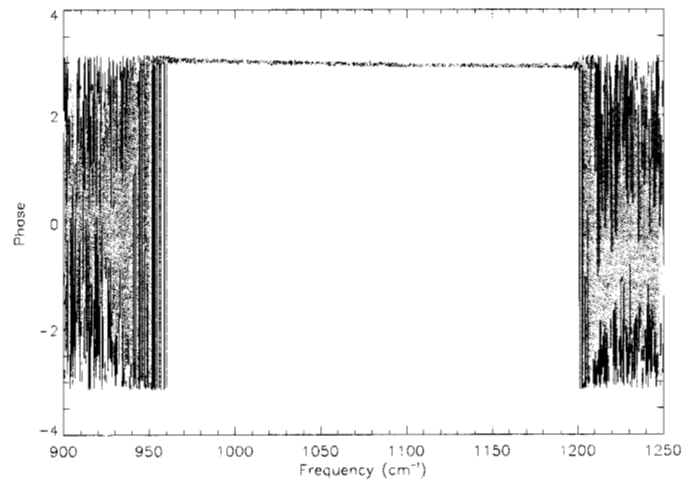


Figure 5.3: Calibration phase alignment of an AES 340 K blackbody. After phase alignment the aligned blackbody phase, which is green, is shown superimposed over the reference blackbody phase, which is black.

Currently the technique for finding the minima of Equations (5.5) and (5.6) is to loop through k . The maximum range of k will be determined during the commissioning phase of the instrument. Within a run, the minimum value of χ should be approximately the same for all of scans. If this minimum value of a particular scan deviates significantly from the average of the run, then the search for a minimum $\chi(k)$ will be performed again with a larger range of k (excluding, of course, the previously calculated values of k).

5.3 Time interpolation of calibration spectra

Since science and calibration data are not acquired simultaneously, time interpolation must be performed so that calibrations can be applied to science measurements taken at different times. We expect the instrument offset radiance, (and possibly the instrument response as well), to vary with time, therefore, all of our operating scenarios involve taking calibration data before and after our target data. At present, we are planning to take single cold-space and blackbody calibration scans alternating with our limb and nadir target observations during our 4-day cycle (58 orbits) in the Global Survey mode. We will also have a set of multiple calibration scans before and after each 4-day cycle. Once the on-orbit offset and response variations are characterized, the time interpolation algorithm will need to optimize the number of calibrations that could be averaged or combined in a fit in order to increase the calibration SNR, while still representing the time variability.

Our current best estimate of the instrument temperature variation during orbit is for the PCS (pointing control system) gimbal mirror which has a maximum change of 1.2K over the orbit and follows a relatively smooth heating and cooling cycle. The model used to predict the orbital temperature variation included the solar flux incident on the back of the PCS gimbal near the orbit terminator as well as the earth's emitted and reflected radiance, (J. Rodriguez, personal communication). The secondary mirror in the PCS should only vary about 30% of this amplitude and all other foreoptics and interferometer components are expected to have negligible temperature variations. This means the instrument offset radiance should change only slightly over the orbit and should have a smooth variation that will allow us to perform either averaging of calibration spectra or a fit to the orbital variation in the calibration signal levels.

During the commissioning phase of TES, we will perform many calibrations to determine the actual orbital variation of the instrument offset and response. If the offset variations are repeatable from one orbit to the next (at least for a 4-

day global survey) then a reasonable approach to increasing the calibration SNR would be to average calibration spectra taken at the same latitudes, or equivalently, the same times from orbit start. This would allow averages of at least 58 spectra, which is sufficient for reducing the noise contribution of the calibration spectra to the final calibrated radiance to less than 2% of the noise from the spectrum being calibrated.

As a default, we can perform a simple linear interpolation in time to compute the calibration spectra to be used in the radiometric calibration for the time of the target data acquisition. (If we are able to perform averaging of calibration spectra taken at the same times from orbit start, then this becomes interpolation with respect to time from orbit start rather than absolute time.) Assuming the target spectrum was taken at time t , and the calibration spectra (blackbody or cold space calibration view) were taken at times $t_1 < t$ and $t_2 > t$, the approximate calibration spectrum at time t is

$$C_{cal}(t) = f_1 C_{cal}(t_1) + f_2 C_{cal}(t_2) \text{ with } f_1 + f_2 = 1.0, f_1 = \frac{t_2 - t}{t_2 - t_1}. \quad (5.7)$$

5.4 Frequency scale determination

Up to this point, the transformations to our data have been independent of the spectral frequency ranges that are associated with the particular sampling rate, alias band and optical filter used when recording TES interferograms. A frequency value for each spectral point must now be determined in order to perform the radiometric calibration since we must calculate the Planck function for the calibration spectra. These frequency scales will be determined using the the estimated laser frequency that is routinely updated in the spectral calibration utility. However, a more precise spectral calibration will still need to be performed later, and is described in Chapter (7).

The frequency scale is calculated from the frequency of the laser used to control interferogram sampling, ν_l , as follows:

$$\nu_{min} = \frac{\nu_l}{2N_{step}}(N_{alias} - 1) \quad (5.8)$$

$$\nu_{max} = \frac{\nu_l}{2N_{step}}N_{alias}, \quad (5.9)$$

where N_{step} is the integral sampling step, *i.e.*, number of laser fringes per interferogram sample, and N_{alias} is the integral alias number corresponding to the sampling step and the spectral interval allowed by the optical filter bandpass. (These

numbers are filter dependent). The frequency spacing of the spectral array is

$$\delta\nu = \frac{\nu_l}{2N_{step}(N_{pts} - 1)}, \quad (5.10)$$

where N_{pts} is the number of spectral points, which will vary according to the sampling step size and the type of transform from interferogram to spectrum, *i.e.*, power of 2 FFT or prime-factor FFT.

We must also account for the change in frequency due to the off-axis angles subtended by our detectors discussed in Chapter (6). The frequency compression factor, $\rho = \Delta\nu/\nu$, is a constant for each off-axis pixel. Since there are 16 off-axis pixels per detector array and 4 detector arrays, we will need to compute 64 different frequency scales. We can compute estimates for ρ given the expected geometry, shown in Figure (6.1). However, these compression factors will need to be recomputed once actual pixel positions, sizes and uniformities are measured. Since the off-axis frequency shift is always toward lower frequency, *i.e.*, a spectral feature will appear at $\nu' = \nu(1 - \rho)$ in the uncorrected scale but should be at ν , we must adjust the frequency arrays by scaling to higher frequencies. This can be done by applying a pixel dependent “effective” laser frequency in the above equations:

$$\nu_l^{effective} = \frac{\nu_l}{(1 - \rho)}. \quad (5.11)$$

5.5 Calculation of radiometrically calibrated spectra

If we could assume that the sampling phase ($2\pi m\nu/\nu_l$) (see Equation (5.4)) was the same for all measurements, and all other quantities were either constant with time or the measured spectra were correctly time interpolated to the same time coordinate, then we could remove the interferometer emission and its phase by taking the difference of the spectra:

$$C_H(\nu) - C_C(\nu) = r(\nu)\epsilon_{BB}(\nu) (B(\nu, T_H) - B(\nu, T_C)) e^{i\phi(\nu)} e^{i2\pi m\nu/\nu_l} \quad (5.12)$$

$$= r(\nu)\epsilon_{BB}(\nu)B(\nu, T_H) e^{i\phi(\nu)} e^{i2\pi m\nu/\nu_l} \text{ for } C_C = C_{cs}, \quad (5.13)$$

where C_H is the complex spectrum from a “hot” calibration source at temperature T_H and C_C is the complex spectrum from a “cold” calibration source at temperature T_C . This differencing is also done for the science target spectrum:

$$C_{target}(\nu) - C_C(\nu) = r(\nu) (L_{target}(\nu) - \epsilon_{BB}(\nu)B(\nu, T_C)) e^{i\phi(\nu)} e^{i2\pi\nu\nu_l/\nu_l} \quad (5.14)$$

$$= r(\nu) L_{target}(\nu) e^{i\phi(\nu)} e^{i2\pi\nu\nu_l/\nu_l} \text{ for } C_C = C_{cs} \quad (5.15)$$

Normally, $C_C = C_{cs}$, the cold space measurement, however, this calibration procedure would work with any two measurements of calibration sources at different temperatures, provided the optical path through the instrument is the same for the target and all calibration sources. The instrument and sampling phase should then cancel for the ratio of these differenced spectra. This method of calibration was first described by [Revercomb *et al.*, 1988] and also used in [Weddigen *et al.*, 1993] and [Blom *et al.*, 1996]. Solving for $L_{target}(\nu)$ gives

$$L_{target}^{cal}(\nu) = \frac{C_{target}(\nu) - C_C(\nu)}{C_H(\nu) - C_C(\nu)} \epsilon_{BB}(\nu) (B(\nu, T_H) - B(\nu, T_C)) + \epsilon_{BB}(\nu) B(\nu, T_C) \quad (5.16)$$

$$= \frac{C_{target}(\nu) - C_{cs}(\nu)}{C_H(\nu) - C_{cs}(\nu)} \epsilon_{BB}(\nu) B(\nu, T_H) \text{ for } C_C = C_{cs}. \quad (5.17)$$

Note that L_{target}^{cal} is still complex. The real part of the calibrated target radiance, $\text{Re}(L_{target}^{cal})$, is the reported calibrated radiance spectrum, while the imaginary part of the target radiance, $\text{Im}(L_{target}^{cal})$, should contain only noise and is used to estimate the NESR (Noise Equivalent Spectral Radiance, see Section (5.6)) as well as a diagnostic for the calibration procedure.

5.5.1 Target spectrum phase alignment

As was suggested in Section (5.5), the phase of the target spectrum must be aligned to both the phase of the cold space and blackbody calibration spectra. The phases of the blackbody spectra are already aligned within a run using the algorithm discussed in Section (5.2). The same is true for cold space spectra. The phases of the resulting averaged blackbody and cold space spectra are not aligned to each other, however. The target spectrum and the averaged cold space spectrum can be aligned to the averaged blackbody spectrum by minimizing the following equation:

$$\chi_{tar}(k, l) = \left\| M_{spike}(\nu) \text{Im} \left(\frac{C_{target}(\nu) e^{-i2\pi k\nu/\nu_l} - C_C(\nu) e^{-i2\pi l\nu/\nu_l}}{C_H(\nu) - C_C(\nu) e^{-i2\pi l\nu/\nu_l}} \right) \right\|^2, \quad (5.18)$$

where k and l are integers. Equation (5.18) is minimized when the cold space phase has been aligned to the blackbody phase and the target phase has been aligned to the cold space phase. When this alignment occurs, all of the fixed radiances, such as the beam self-emission and the foreoptics, are removed in the difference and the instrument phase $\phi(\nu)$ is removed in the quotient. Thus, the additive fixed radiances are subtracted out and the phase of the target is corrected at the same time. Once the minimum of $\chi_{tar}(k, l)$ is found, the quotient inside the norm $|| \cdot ||^2$ can be substituted into Equation (5.17) to compute the calibrated target radiance. An example of this approach with AES target data is shown in Figure (5.4). Equation (5.18) was applied to the target spectrum along with a 340 K and a 290 K blackbody spectra. Once the minimum was found, the target spectrum was calibrated using Equation (5.17).

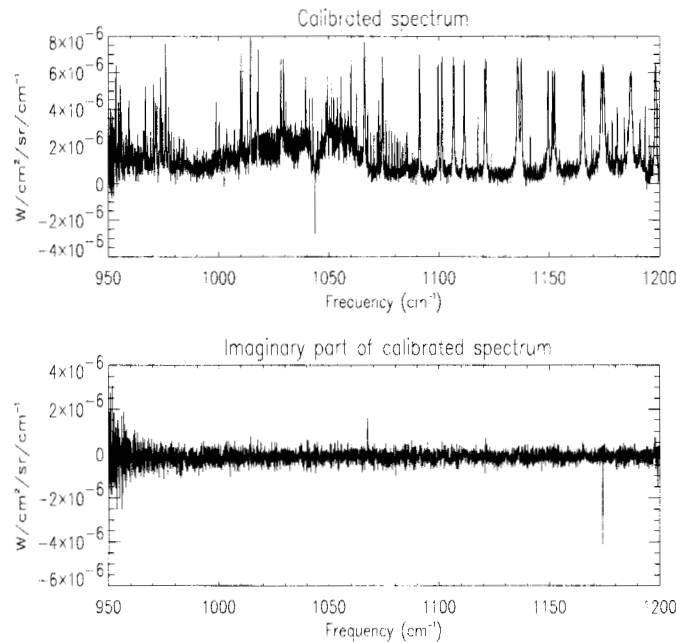


Figure 5.4: Real and imaginary components of a AES calibrated spectrum. When properly aligned, the imaginary component can be approximated as white noise within the pass-band of the optical filter. The increase in values toward the lower frequencies is due to the edges of the optical filter. (Note: spikes in the data have not been removed.)

As in Section (5.2) the technique for finding the minima of Equations (5.5) and (5.6) is to loop through k and l . The maximum range of k and l will be determined during the commissioning phase of the instrument. The minimum value of χ_{tar} should be approximately the same for all scans. If this minimum value for a particular scan deviates significantly from an average calculated over many scans, then the search for a minimum $\chi_{tar}(k, l)$ will be performed again with a larger range of k and l .

A critical assumption for target phase alignment is that the non-linear instrument phase is fixed, or at least any variation can be accurately modeled with time-interpolation as described in Section (5.3). If this assumption is not true, then other phase correction techniques must be used, which are discussed in Appendix (B).

5.5.2 Limb view calibration

The current plan for TES normal operations is to acquire all calibration scans at the nadir resolution: 8.45 cm maximum optical path difference (OPD), in order to optimize observation time. The nadir resolution calibrations are then applied to both nadir and limb science spectra. Although we expect spectral features in the calibration spectra to be broader than the nadir resolution, (and therefore much broader than the limb resolution), this assumption will have to be tested and special calibration sequences taken at the limb resolution (33.8 cm maximum OPD) will be performed as needed during “off” days. In addition to assessing the validity of interpolating low resolution calibrations and applying them to high resolution data, these higher resolution calibrations will be used to determine the appropriate interpolation function. Sources of spectral structure in the limb-resolution calibration data include the optical filter response, possible fine resolution channeling features and absorption lines if there is significant out-gassing of the instrument.

We will implement a straight-forward interpolation to the higher (limb) resolution, unless high resolution calibration scans give information showing this to be insufficient. The interpolation could be done by transforming the sampling phase aligned and averaged complex calibration spectra to interferogram space, zero-padding the interferograms to 4 times the resolution and transforming back to spectral space. Time interpolation and target spectrum phase alignment would then proceed as for the nadir scans.

Interpolating from low resolution to high resolution calibration spectra will necessarily introduce spectral correlation into the calibrated limb spectrum. If the calibration SNR is high enough, these correlations are negligible. Otherwise, they

must be included in the measurement covariance matrix where the diagonal is the NESR, which is discussed in Section (5.6). Although we plan to optimize the calibration SNR in our time interpolation algorithm, we will need to evaluate this correlation once we have actual data.

5.6 NESR estimation

In order to provide Level 2 with an estimate of the random errors in our measured radiance spectra, we need to compute the NESR (noise equivalent spectral radiance) for our science spectra. For source limited noise regime, the NESR must be estimated for each spectrum. In this case, the NESR is estimated by calculating the product of the root-mean-square of the spectrum measured outside of the optical band-pass and the slope of the system response, which is determined from radiometric calibration. The NESR will be estimated for the black-body and cold-space view as well for diagnostic purposes.

This estimation technique will be checked for each spectral point by calculating the standard deviation of the complex component of the spectrum after complex calibration. Assuming that the complex calibration is performed correctly and the phase terms cancel, all of the target signal should be in the real part of the complex calibrated spectrum leaving a noise-like imaginary with a frequency dependent amplitude. (See Figure (5.4) as an example.) The calibrated radiance noise amplitude is frequency dependent due to the shape of the measured calibration spectra, especially at the edges of the optical filters where the signal levels drop significantly. For target scenes of similar radiance levels, calibrated with the same number of averaged calibration spectra, we can estimate the NESR as the standard deviation of an ensemble of calibrated spectral imaginary terms. At each frequency point ν the standard deviation is

$$\sigma(\nu) = \sqrt{\frac{1}{N} \sum_{i=1}^N (\text{Im}(L_i(\nu)) - \overline{\text{Im}(L(\nu))})^2}, \quad (5.19)$$

where $\overline{\text{Im}(L(\nu))}$ is the mean value of the calibrated spectral imaginary terms $\text{Im}(L_i(\nu))$.

Since the mean value used to determine $\sigma(\nu)$ has an error of $\sigma(\nu)/\sqrt{N}$, we need the number of measurements, N , to be large enough, say at least 100, in order to have an accurate estimate of the NESR.

5.7 Systematic errors

Systematic errors in the radiometric calibration for TES will result from uncertainties in the blackbody temperature and/or emissivity, angular dependence of the optical properties of the pointing mirror and invalid assumptions about the time variability of the instrument offset and slope when performing time interpolations of the calibration spectra.

The TES calibration blackbody will be a cavity blackbody with temperature measured by platinum resistance thermometers (PRTs). We expect these to have an accuracy of 0.1 K and precision better than 0.01 K. The emissivity of the blackbody should be greater than 0.9995. From these expected values we can estimate the systematic error in radiance and apparent brightness temperature. For a 0.1 K error in the blackbody temperature, the corresponding error in radiance increases from about 0.1% at 650 cm^{-1} to 0.3% at 2500 cm^{-1} . For a target scene at 300 K, this gives an error of 0.08 K in the apparent brightness temperature. Errors in the assumed emissivity will produce a radiance error that is constant in frequency but apparent brightness temperature errors that vary with frequency. For an emissivity error of 0.1%, the maximum error in brightness temperature is around 0.09 K at 650 cm^{-1} .

Although the pointing mirror has been designed so that it has no angular dependence (the mirror has no overcoat that would introduce polarization), there is always some possibility that scattering could cause a slight angular dependence. If there were such a dependence, it would affect the relative signal levels at different angles. This would lead to a systematic error in the spectral radiance since the most basic assumption in our calibration is that the transmission through the instrument is the same for both calibration and target scenes, which are viewed at different angles of the pointing mirror. The angular dependence of the pointing mirror will be tested and characterized both before and after launch.

The assumptions we make about time variability in the instrument response and offset will be based on our initial measurements in orbit from both our calibration spectra and the temperature sensor measurements of different instrument components. The calibration strategy used in these initial measurements will account for the expected variations from models of the thermal response of various components, but will probably be modified once real data are acquired. After we have a better understanding of how the response and offset change with time, we can optimize the trade-off between averaging calibrations for an improved SNR and minimizing the systematic errors incurred by the time interpolation.

Systematic errors will be estimated offline and stored so that they are reported

with the measured radiances along with the NESR.

5.8 Algorithm validation

The Level 1B radiometric calibration algorithms will be validated using simulations and data from the Airborne Emission Spectrometer (AES), TES protoflight calibrations and TES itself. Simulations of nadir, limb and blackbody spectra already exist for the testing of algorithm components and will be used to generate more complete TES simulated data sets for end-to-end testing.

A standard test for validation of the time interpolation and radiance calculation uses blackbody measurements taken at three different temperatures and should be performed with all of the data sets. The high and low temperature spectra are used to generate the calibration spectra at the time of the middle temperature measurement. The middle temperature spectrum is then calibrated and should have a radiance that corresponds to the known temperature.

For validation of the limb spectra calibration, a similar test can be performed using high and low temperature spectra at nadir resolution and a limb resolution blackbody spectrum taken at a middle temperature.

In the laboratory, the cold-space calibration view can be simulated by a dewar of liquid nitrogen. In this case, the source radiance is negligible and the detected signal is due to the instrument radiance. We could then test the calibration using this “cold-space” view and a blackbody at 340 K compared to using two different blackbody temperatures.

Chapter 6

Off-axis ILS Correction and Modeling

6.1 Introduction

In an ideal Fourier transform spectrometer, an interferogram is measured with an on-axis point detector. In this case, there is a simple, linear relationship between the distance traversed by one arm of the interferometer and the optical path of the incident radiation. For a detector of finite dimensions and positioned off-axis, however, the relationship between the interferometer arm length and the optical path of a ray becomes more complicated.

Figure (6.1) shows the path of a ray to a pixel positioned off-axis. The output of the detector is equal to the integral over all incident rays and over all wavelengths. The resulting interferogram is written as

$$I(x) = \int_{-\beta_w}^{\beta_w} \int_{\alpha_i}^{\alpha_{i+1}} \left[\int_{-\infty}^{\infty} P(\alpha, \beta) L(v) e^{-i2\pi \cos(\phi(\alpha, \beta)) vx} dv \right] d\alpha d\beta, \quad (6.1)$$

where $P(\alpha, \beta)$ is the angular response of the detector, $L(v)$ is the input spectrum, α_i and α_{i+1} are the angles to the lower and upper edge of the i th pixel, and β_w is the angle to the maximum horizontal extent of the pixel. The angle of a ray, denoted by ϕ , is related to the angles α and β by

$$\tan^2 \phi = \tan^2 \alpha + \tan^2 \beta. \quad (6.2)$$

Equation (6.1) can be interpreted as an interferogram that is equal to a sum of interferograms generated by each ray of incident radiance. Thus, a given distance

traversed by the interferometer arm, say \bar{x} , now corresponds to rays summed over slightly different optical paths.

The off-axis geometry shown in Figure (6.1) alters the input spectrum in several ways that is not readily apparent from an inspection of Equation (6.1). Figure (6.2)(a) shows the interferogram of a simulated monochromatic input radiance at $\nu = 2461.5 \text{ cm}^{-1}$ measured off-axis. The limb case is assumed so that the maximum OPD is $x = 33.78784 \text{ cm}$. The angles correspond to pixel 8, which is the pixel farthest from the optical axis. Figure (6.2)(b) shows the Fourier transform of the off-axis interferogram. For simplicity, the off-axis angular response, $P(\alpha, \beta)$, is set to unity. The interferogram in Figure (6.2)(a) appears to be a cosinusoid modulated by some envelope function. The interferogram is referred to as being “self-apodized” since the off-axis geometry itself appears to impose an apodization function¹ on the interferogram. The self-apodization of the interferogram results in a ILS that is broadened in frequency and reduced in amplitude, as shown in Figure (6.2)(b). In addition, the ILS appears to be shifted in frequency and the side-lobes of the ILS are asymmetric. These four characteristics are deviations from the monochromatic input radiance measured on-axis.

6.2 Fresnel approximation

With some simplifying assumptions on Equation (6.1), these off-axis effects can be isolated and understood. Equation (6.2) can be approximated by

$$\phi^2 \approx \alpha^2 + \beta^2, \quad (6.3)$$

and thus

$$\cos \phi(\alpha, \beta) \approx 1 - \frac{\alpha^2 + \beta^2}{2}. \quad (6.4)$$

Substituting Equation (6.4) into Equation (6.1) and with some additional manipulations results in [Bowman, 1997]

$$I(x) \approx 2\text{Re} \left\{ \int_{\nu_F} L(\nu) A(\nu x) e^{-i2\pi\nu x} d\nu \right\}, \quad (6.5)$$

¹The term “apodization” was originally coined to mean the removal of false sidelobes in a transformed spectrum introduced by measuring only a finite number of optical path differences. “apod” means having no feet [Bell, 1972].

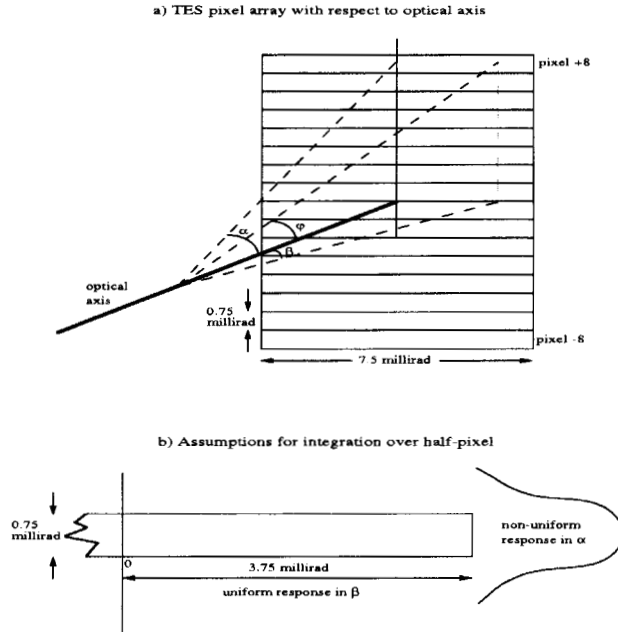


Figure 6.1: Off-axis geometry

where

$$A(vx) = \int_{-\beta_w}^{\beta_w} \int_{\alpha_i}^{\alpha_{i+1}} P(\alpha, \beta) e^{i2\pi\alpha^2 vx} e^{i2\pi\beta^2 vx} d\alpha d\beta. \quad (6.6)$$

The function $A(vx)$ is called the *Fresnel kernel*. An analysis of the Fresnel kernel will divulge the observed properties of the off-axis interferogram and spectrum.

The Fresnel kernel can be written in phaser form as

$$A(vx) = |A(vx)| e^{i\Phi(vx)}. \quad (6.7)$$

For $v = 2537.5 \text{ cm}^{-1}$, the magnitude and phase of the Fresnel kernel is shown in Figure (6.3). The magnitude of the Fresnel kernel in Figure (6.3)(a) corresponds to the envelope or “self-apodization” of the off-axis interferogram shown in Figure (6.2). Hence, the Fresnel magnitude function is called the *self-apodization function*. The phase function of the Fresnel kernel, shown in Figure (6.3)(b) is dominated by a linear term. The slope of this term corresponds to the frequency shift shown in Figure (6.2)(b).

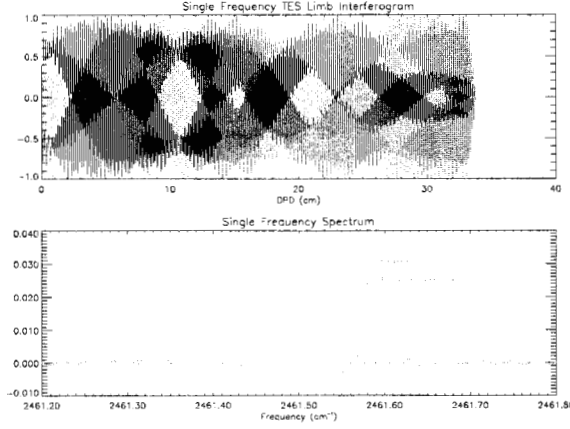


Figure 6.2: Simulated off-axis interferogram and the resultant ILS.

This phase function, however, is non-linear. The Fresnel phase function can be decomposed into linear and non-linear components, denoted as

$$\Phi(vx) = 2\pi\rho vx + \psi(vx). \quad (6.8)$$

Substituting Equation (6.7) and Equation (6.8) into Equation (6.5) leads to

$$I(x) = 2\text{Re} \left\{ \int_{\mathcal{V}_F} |A(vx)| e^{i\psi(vx)} L(v) e^{-i2\pi(1-\rho)vx} dv \right\}. \quad (6.9)$$

For a sufficiently narrow band spectrum, Equation (6.9) becomes

$$I(x) = 2|A(\bar{v}x)| \text{Re} \left\{ e^{i\psi(\bar{v}x)} \int_0^\infty L(\bar{v}) e^{-i2\pi(1-\rho)\bar{v}x} d\bar{v} \right\} \quad (6.10)$$

$$= 2|A(\bar{v}x)| \text{Re} \left\{ e^{i\psi(\bar{v}x)} I_F \left(\frac{x}{1-\rho} \right) \right\} \quad (6.11)$$

The first term in Equation (6.10) is the self-apodization function and the second term represents the non-linear portion of the Fresnel phase function. This phase function, $\psi(\bar{v}x)$, is called the *residual Fresnel phase function* or simply the *residual phase function*. The residual phase function is shown in Figure (6.4)(a). The term $e^{i\psi(\bar{v}x)}$ is treated as a complex ILS function and is called the *residual ILS function*. The Fourier transform of the residual ILS function is shown in Figure (6.4)(b). The side-lobes depicted in Figure (6.4)(b) are asymmetric.

Hence the convolution of the Fourier transform of the residual ILS function with a monochromatic input will also result in asymmetric side-lobes of the spectrum as shown in Figure (6.2)(b). Inside the integral of Equation (6.10) the frequency variable ν is multiplied by $1 - \rho$. The spectrum, then, is scaled by the factor $1/(1 - \rho)$. The slope of the Fresnel phase function, ρ , is also called the *compression factor* and the term $(1 - \rho)$ is the *off-axis scale factor*. What appears to be a shift in Figure (6.2)(b) is actually a scaling.

The Fresnel kernel described in Equation (6.6) and in Equation (6.10) capture the observed features of off-axis spectra:

- the magnitude of the Fresnel kernel describes the envelope of the interferogram as well as the broadening and the decrease in amplitude of the spectrum,
- the non-linear phase term of the Fresnel kernel describes the asymmetry of the spectrum,
- the linear phase term of the Fresnel kernel describes the scaling of the input radiance.

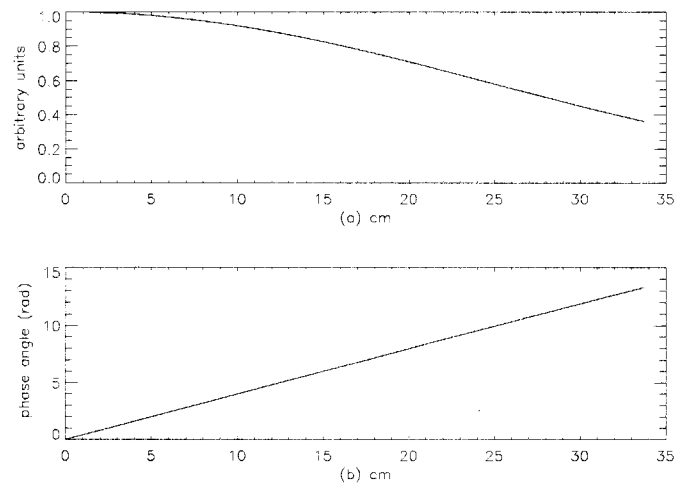


Figure 6.3: (a) The magnitude of the Fresnel kernel (b) the phase of the Fresnel kernel for $\nu = 2461.5 \text{ cm}^{-1}$

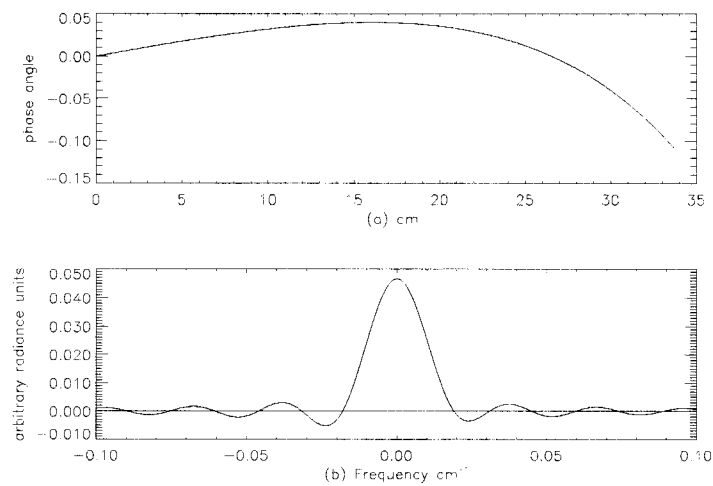


Figure 6.4: (a) The residual Fresnel phase function (b) The Fourier transform of the residual Fresnel phase function

6.3 Validation for broad band spectra

For a sufficiently narrow band spectrum, the self-apodization term in Equation (6.11) can be simply divided out. The interferogram can be rescaled to remove the off-axis scale factor $(1 - \rho)$ from I_F . The residual ILS function, however, must be modeled in Level 2 because the function is complex. The problem, of course, is that most spectra are *broad* band, not narrow band. Conceptually, the input spectrum, can be split into frequency bands:

$$L(\nu) = L_1(\nu) + L_2(\nu) + \cdots + L_M(\nu), \quad (6.12)$$

where M is the number of bands and $L_n(\nu)$ is non-zero only on the interval $\nu \in [\nu_n, \nu_{n+1}]$. Each of the interferograms, $I_1(x), I_2(x), \dots, I_M(x)$ corresponding to the frequency bands, can be modeled by Equation (6.11). The self-apodization and residual ILS functions are calculated for the frequencies defined by

$$\bar{\nu}_n = \frac{\nu_n + \nu_{n+1}}{2}, \quad (6.13)$$

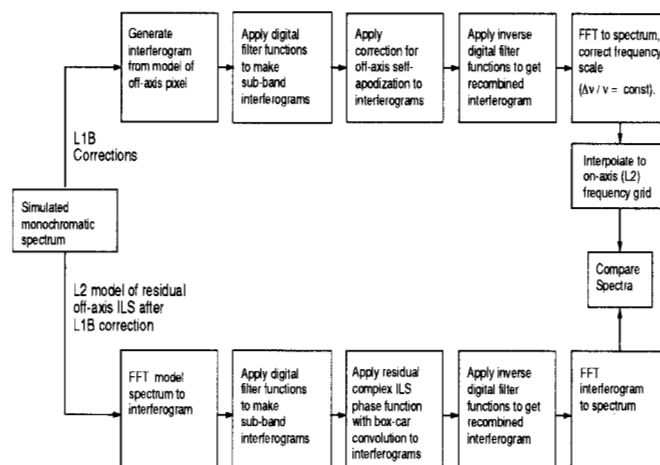
which is the center of the band.

The principle problem, however, is to calculate $I_n(x)$ in the first place. In principle, this interferogram could be obtained by applying an ideal band-pass filter to the measured spectrum. In practice, however, direct implementation of these filters produces excessive ringing. Moreover, a spectrum that is split into frequency bands in this manner can not, in general, be reconstructed from those frequency bands. Nevertheless, there exists an efficient technique known as “filter banks” (or wavelets) that can split a spectrum into bands in such a way as to allow for perfect reconstruction from those bands. This technique is described in Appendix (A.1) and [Bowman *et al.*, 1999].

A testing procedure and description of the off-axis ILS correction and modeling algorithm is shown in Figure (6.5). For the Level 1B correction, the interferogram is split into several several, smaller interferograms that correspond to the frequency bands in Equation (6.12). Each interferogram is then divided by a self-apodization function, which has been calculated for the center of each band. The interferograms are recombined, using filter banks, to produce a single interferogram that has the self-apodization terms removed. This interferogram is then resampled by the off-axis scale factor. The spectrum of the resulting interferogram is interpolated onto the Level 2 frequency grid. For the Level 2 modeling procedure, the forward model interferogram at the instrument resolution is split

into several interferograms with filter banks identical to those used in the Level 1B technique. Each interferogram is then multiplied by a residual ILS function, which was calculated from the center frequency of the filter band. After multiplication, these interferograms are then recombined with filter banks into one forward model interferogram. The spectrum of this interferogram is compared to the spectrum calculated in Level 1B. An example of this algorithm is discussed in Appendix (A.2) and [Bowman *et al.*, 1999].

Test of Off-Axis ILS Correction and Modeling



H Worden 06/22/96

Figure 6.5: Steps for off-axis ILS correction and modeling

6.4 Non-uniform illumination

The previous examples have assumed a known, uniform illumination over the pixel. In practice the actual illumination can vary and is generally not known. To test the sensitivity of the method to illumination errors we calculated a gradient illumination, which was assumed to be constant in the horizontal direction but drops off linearly from one to zero in the vertical direction. This represents a

“worst case” situation, but has similarities to a pixel viewing the tropopause in either its upper or lower edge. Figure (6.6) shows the effective pixel response under gradient illumination. The Fresnel kernel was calculated for both uniform and gradient illumination for 1050 cm^{-1} .

The Fresnel kernel calculated for the gradient illumination was applied to the off-axis spectrum under uniform illumination. The corrections were made over a 5 cm^{-1} window. The errors for the uniformly and gradient illuminated case are shown in Table (6.1). For the uniform case, there are no model errors and thus they establish a baseline. For the gradient case, the error in the Level 1B correction increases by approximately a factor of 2. This error, however, is still considered acceptable. The Level 2 residual correction, on the other hand, is an order of magnitude worse than the Level 1B correction only. In this case, it would be better to not apply the Level 2 residual modelling at all. The explanation for this performance can be seen by examining the change in the self-apodization and residual ILS phase functions, which are shown in Figure (6.7). The self-apodization function has only a slight variation with illumination whereas the residual ILS phase function has changed significantly.

The variation of the illumination appears to change the slope of the residual ILS function. This suggests that the residual ILS function could be parameterized as a function of the field-of-view (FOV) illumination, which is estimated during the retrieval. From the estimated FOV, the residual ILS function could be calculated, leading to a more robust algorithm. The effect of illumination on the ILS underscores the importance of separating the self-apodization correction in Level 1B and the residual modeling in Level 2. The Level 1B correction allows the spectra from all of the pixels to be intercompared even in the presence of non-uniform illumination between the pixels. Modelling the ILS entirely does not allow one to separate those ILS effects insensitive to non-uniform illumination from those effects that are sensitive to non-uniform illumination.

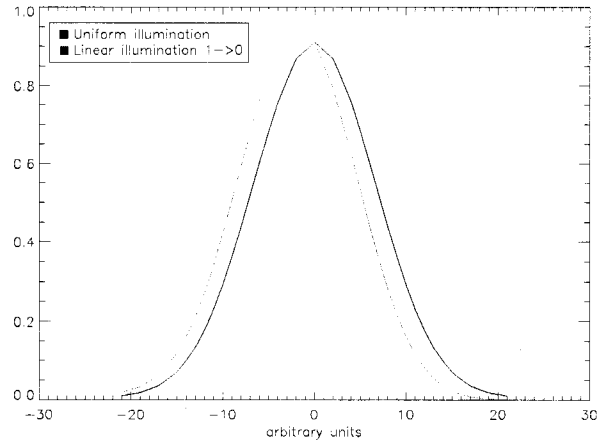


Figure 6.6: Pixel response of the detector under non-uniform and gradient illumination.

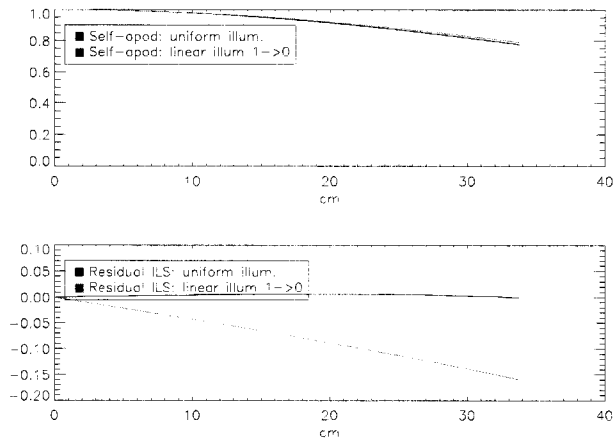


Figure 6.7: The self-apodization functions and residual ILS phase functions under uniform and non-uniform illumination.

Table 6.1: Error levels for ILS correction & modeling processing steps using simulated limb views for pixel 1 (8th off-axis pixel) for both the cases of known (uniform) illumination and illumination mismatch (gradient).

Illumination	Processing step	max. error/ avg. signal
Uniform	on-axis (no L2 model) - L1B	.27%
Uniform	on-axis with L2 model - L1B	0.024%
Gradient	on-axis (no L2 model) - L1B	0.56%
Gradient	on-axis with L2 model - L1B	5.6%

Chapter 7

Spectral Calibration

7.1 Frequency scale adjustments to match model line positions

This chapter describes the corrections to the frequency scales assigned to Level 1B data that are necessary in order for the measured positions of molecular transitions (or “lines”) to match the calculated positions in the spectra generated by the forward model in Level 2. This step must be performed so that the model spectrum can be subtracted from the data in the Level 2 retrieval. Although the measured and calculated line frequencies should be close after applying the frequency scale corrections discussed in this chapter and in Section (5.4), the frequency scales and their corrections are generated from instrument parameters such as the laser frequency, the off-axis pixel positions and the spacecraft velocity, and are subject to uncertainties. Additional corrections are therefore needed to place the TES measured line positions at the transition frequencies in the line-by-line database used to generate the absorption coefficients in the Level 2 model.

For limb data, we must now correct for the Doppler shift. This must be corrected *after* the radiometric calibration since the radiance arriving at the instrument is already Doppler shifted when the instrument offset and response are applied. Therefore we must correct for the Doppler shift after these instrument effects have been removed. The Doppler shift is given by:

$$\frac{\Delta v_{Doppler}}{v} = \frac{v_{TES}}{c} \approx 2.26 \times 10^{-5} \quad (7.1)$$

where c is the speed of light and v_{TES} is the TES velocity relative to the limb view. v_{TES} is computed from the orbital velocity of 7.5 km/sec projected to the

limb viewing angle (64.52°) giving 6.77 km/sec. Since we view the trailing limb, the Doppler shift is always toward lower frequency (just as the off-axis frequency shift). Therefore, for limb spectra, the frequency scale is recomputed using the effective laser frequency given by Equation (5.11) with:

$$\frac{\Delta v}{v} = \frac{\Delta v_{Doppler}}{v} + \frac{\Delta v_{off-axis}}{v} \quad (7.2)$$

At this point, since the off-axis frequency correction is pixel dependent, we will have 64 nadir and 64 limb (16 pixels, 4 dewars/filters) frequency scales that will each have to be adjusted to match the model line positions.

The coefficients for adjusting the frequency scale are calculated using some of the clearly distinguishable and well-measured molecular transitions that should always be present in the TES spectral data. Once the measured frequency for the peak (or minimum) of a particular transition is identified in the spectral data, it can be compared with the database frequency giving a δv for that transition. Using several transitions (or “lines”) will allow a fit to δv as a function of frequency. In general, the fit to δv vs v should be very close to linear since all of our previous corrections, *i.e.*, off-axis and Doppler, have $\delta v/v = \text{constant}$. However, this linearity will need to be verified to assure that our assumptions about the frequency scale calculation are valid.

7.1.1 Line selection

Good candidates for identifiable spectral features are lines that are relatively strong, but not saturated since these could have a poorly defined “peak” frequency. H_2O transitions are also undesirable since the transition frequency can be pressure shifted. This is problematic not only because the database frequency is not a constant for these H_2O transitions, but also because many of the pressure shifts are not well known. CO_2 , N_2O and CO lines are good candidates since they have enough atmospheric abundance to cause clear, visible spectral features, both saturated and unsaturated, in most of the TES filter bands. Where these lines are not present, CH_4 and perhaps weaker H_2O lines will need to be used.

Since nadir spectra and limb spectra will have saturated or obscured spectral lines at different frequencies, the choice of lines to use for a frequency comparison will depend on the viewing mode (limb or nadir) and tangent height of the limb view. An initial list of line candidates for the frequency correction will be created based on model spectra of the nadir view and the limb views at various altitudes that are generated using model atmospheres at different latitudes (*i.e.*

tropical, mid-latitude, arctic) and for different seasons. Since this could be very time consuming to generate for all the limb altitudes, we will start by using the same lines that have been studied for use in the spectral calibration of the MIPAS experiment [Lachance, 1998], at least for the higher limb tangent altitudes. The list of spectral calibration lines will most likely be modified, however, once actual data are acquired and compared with the model spectra.

7.1.2 Determination of frequency shifts

The most difficult aspect of this algorithm is computing the frequency shifts of measured lines relative to the corresponding database transitions. This must be done on a line-by-line basis since the frequency shift could change over the frequency range of a filter band. The most reliable method, as demonstrated in [Beer, 1997], has been to cross-correlate the data spectrum with a model. This gives a correlation peak at the shift frequency where the data and model have the best match. Another option is to simply find the frequency at the peak of the spectral line itself using a peak-finding routine, however, spectral features can have a variety of backgrounds such as a sloping radiance curve or a wider, saturated feature under the sharper peak. Finding the frequency shift of the correlation peak allows a more robust method of peak finding since the resulting curve is more consistent.

The correlation of a data spectrum R and model spectrum F at a frequency ν' is given by:

$$C(\nu') = \int_{-\infty}^{\infty} R(\nu)F(\nu' + \nu)d\nu \quad (7.3)$$

An efficient way of computing this integral uses the Fourier transform, denoted by $\xleftrightarrow{\mathcal{F}}$:

$$C(\nu') \xleftrightarrow{\mathcal{F}} (I_R^* I_F) \quad (7.4)$$

where I_R^* is the complex conjugate of $I_R \xleftrightarrow{\mathcal{F}} R$ and $I_F \xleftrightarrow{\mathcal{F}} F$.

This correlation is calculated for frequency shifts up to \pm TBD for each line frequency in the list of lines used for spectral correction. The frequency shift at the peak of the correlation curve is found using a center-of-gravity (CoG) peak finding algorithm [Cameron *et al.*, 1982]. This method gives the peak frequency, ν_{cg} as:

$$\nu_{cg} = 0.5\Delta\nu \left[\frac{\sum_{i=j}^k i(C_i - C_k)}{\sum_{i=j}^k (C_i - C_k)} + \frac{\sum_{i=j}^{k-1} i(C_i - C_j)}{\sum_{i=j}^{k-1} (C_i - C_j)} \right] \quad (7.5)$$

where Δv is the spacing of the frequency grid and C is the correlation peak array. Indices j and k are defined in terms of the fraction f of the peak that is used. Let $C_f = fC_{max}$ then k is the index where C_k is closest to C_f but with $k > i_{max}$ and j is the index that satisfies $j < i_{max}$ and C_j closest to C_f but $C_j \geq C_k$. The fraction f must be chosen to include enough points without including much of the background under the peak. The error in frequency from this fit is given by:

$$dv = \frac{\Delta v \sum_{i=j}^k i N_i}{\sum_{i=j}^k (C_i - C_f)} \quad (7.6)$$

An alternate approach to using a center-of-gravity peak finder is to apply the Fourier shift theorem (described in many textbooks [Jansson, 1984]). As with the CoG method, some fraction of the points in the peak are used. The array of this fraction of points is shifted so that the point corresponding to maximum value is at zero index. The additional frequency shift at the peak is calculated by performing a FFT of the array, and fitting the phase (arctangent of the imaginary part over the real part) to a straight line. For a reasonably symmetric peak, the phase should have a zero offset. The frequency shift is given by:

$$\delta v = -\frac{\text{slope}}{2\pi} \quad (7.7)$$

Care must be taken in choosing the fraction of the peak, using the right abscissa in the fit to the slope, and fitting only the portion of the phase where there is sufficient signal for the phase determination. The error in the frequency shift is given by the RMS residual of the linear fit for the slope (divided by 2π).

If the frequency shift were constant over a large spectral region (e.g., any of the TES filter bands), a simple algorithm to measure it would be to compute the correlation curve for several lines simultaneously, and using the Fourier shift theorem, extract the frequency shift over the spectral region. However, in AES data the frequency shift is not a constant over a filter band, and a linear fit to the frequency shifts of individual lines as a function of frequency is performed in order to adjust the frequency scale to match model line frequencies. The coefficients from this fit can be thought of as a frequency offset and "stretch". Figures (7.1) and (7.2) show examples of the frequency scale correction and the correlation curve for a single CO₂ line from AES data.

Since some of the spectral features will have a better SNR than others, the individual frequency shifts should be weighted by their errors in the peak position, either with the error from the CoG fit (which is estimated from the spectral noise levels) or the error from the Fourier shift theorem method.

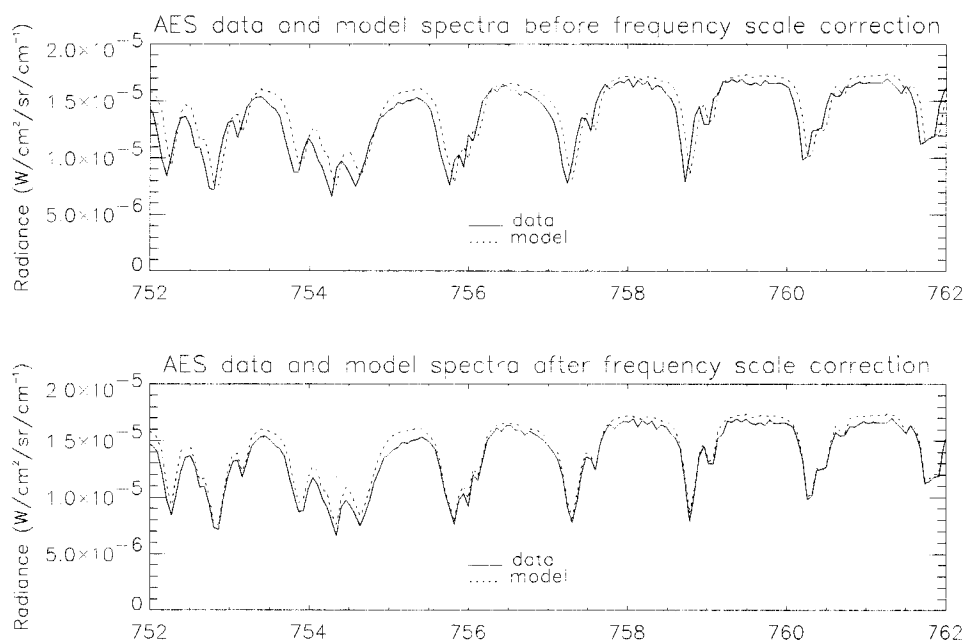


Figure 7.1: Example of the frequency scale correction using CO_2 lines in AES data with a model spectrum generated using atmospheric profiles of temperature and humidity from a radiosonde and the current mean CO_2 abundance. The AES spectrum is an average of 234 spectra from individual scans, and has a SNR of about 120 in this spectral region.

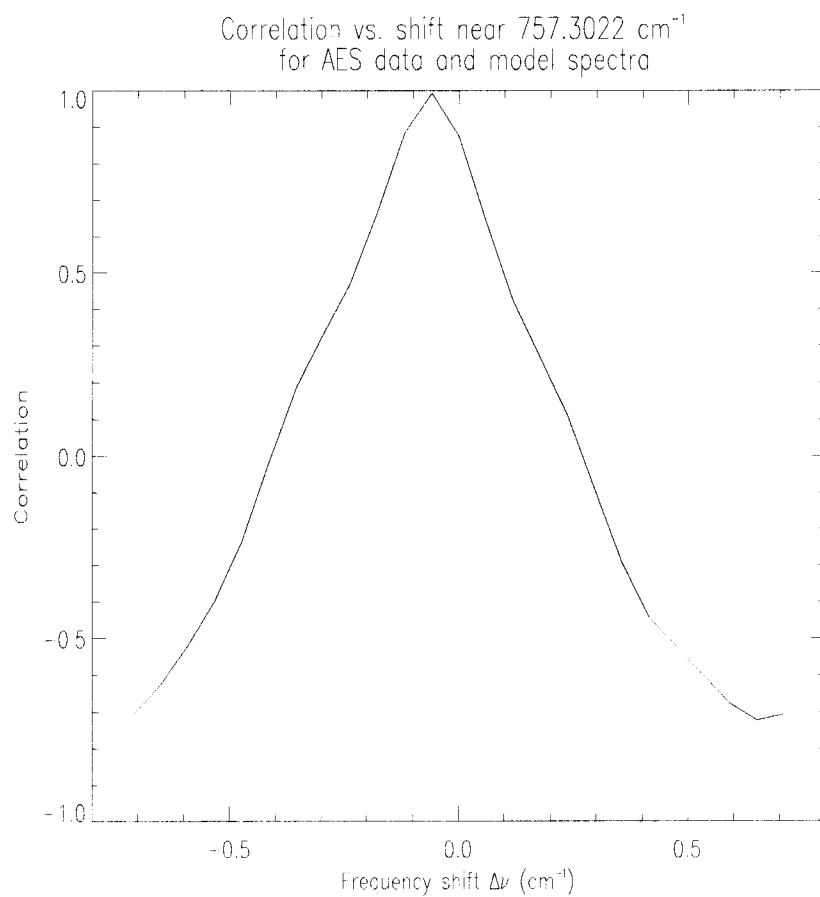


Figure 7.2: Correlation vs. frequency shift near a CO_2 line for the AES data and model spectra in Figure (7.1)

7.2 Resampling to the common L2 frequency grid

The final step in the Level 1B process is to prepare the spectra for input to Level 2 (L2) retrievals. As discussed in Section (5.4), each pixel will have a slightly different frequency grid. In addition to simplifying inputs to the L2 algorithm, resampling these frequency grids so that spectra from different pixels are on a common frequency grid will allow averaging of spectra as a pre-processing step, if necessary, and also comparisons of the spectral features in the different pixels.

Although we are investigating methods that should be less time consuming, at present, we have a slow, but robust interpolation method that introduces small, but acceptable errors in the radiance spectra. In this method, the spectra are interpolated by performing an FFT to interferogram space, center zero-padding the interferogram array to a size 2^N , where N is an integer and the zero-padded array size is much larger than the original spectral array size, performing an FFT to spectral space and then selecting the 2 closest points in frequency to the on-axis frequency grid from the much more finely spaced interpolated grid. The resulting spectrum is the proximity-weighted average of the two closest points in the finely sampled spectrum.

Numerical errors in the interpolation begin to converge so that increased array size does not improve the difference between the on-axis “true” spectrum and the corrected, interpolated “off-axis” spectrum. The main source of error not associated with the frequency spacing is the “ringing” resulting from the sharp cutoff at the end of the interferogram. This is evident in Figure (7.3) which shows the differences between a corrected and interpolated frequency shifted monochromatic spectrum and the corresponding “on-axis” spectrum for a non-apodized and apodized case. It is clear that apodization significantly reduces the “ringing”.

7.3 Algorithm validation

The spectral calibration algorithm has been verified using AES data; however, an automated method needs to be developed to check for errors.

The resampling/interpolation algorithm has been validated separately for individual lines (see Figure (7.3)) and in the context of the ILS correction/modelling algorithm (Section (6.3)) for a simulated limb spectrum. In both cases, the errors are well below our stated goal of 0.1%.

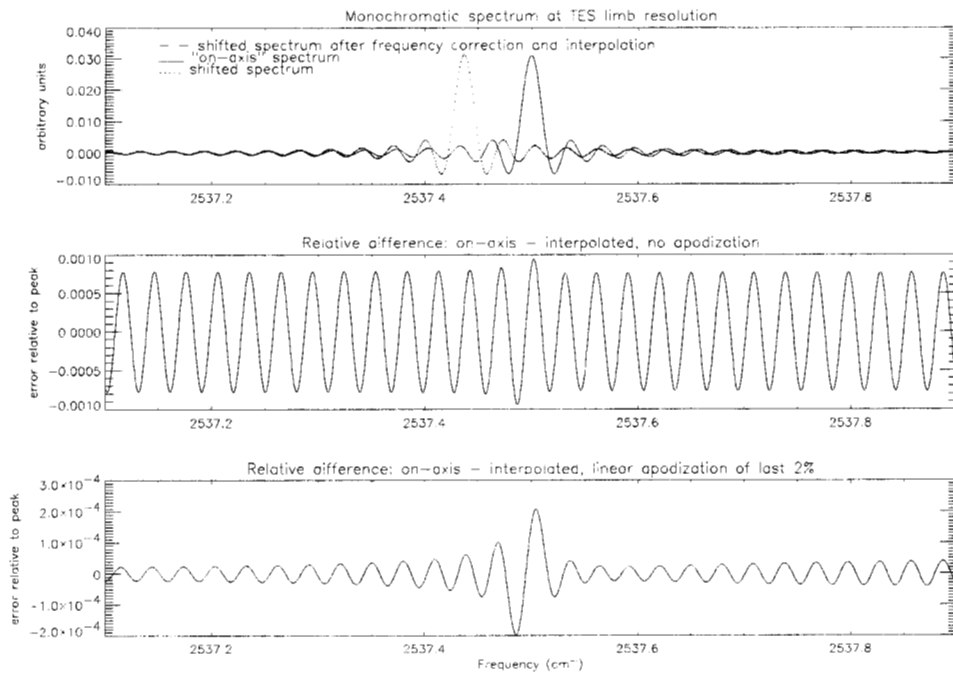


Figure 7.3: Error levels after frequency correction and interpolation for the cases where no apodization is performed (center) and where a linear apodization is performed on the last 2% of the interferogram, before zero-padding (bottom).

Chapter 8

Data Quality Assessment

8.1 Introduction

In this chapter we will identify some of the data quality flags that will be attached to the Level 1B data (in addition to flags from Level 1A) and considered by Level 2 before further processing. There are two types of quality flags:

1) Scene quality flags: These relate to either cloudy or anomalous scenes that can be flagged by level 1B and would require either special processing by level 2 or would not be processed further. Assuming nadir pixels are averaged in level 2 operational processing, these flags will apply to all of the spectra taken of the particular scene, (i.e. all the pixels and filters used in the scan). For limb data, all of the filters, but only pixels at and below any cloud contaminated pixel would be flagged.

2) Data quality flags: These relate to instrument and/or processing errors that have either corrupted or degraded the data past the point of being usable in level 2. These may apply to individual spectra and pixels or to all of the spectra in a scan, depending on the error.

8.2 Cloud and anomaly detection

Since nadir scenes have a much broader range of possible background radiances, the nadir cloud detection algorithm will necessarily be more complex than the algorithm for limb cloud detection. For limb data from the upper troposphere and above, where there is only a small continuum contribution for the clear sky case, a simple radiance or brightness temperature threshold technique in the $12\mu\text{m}$

window region should be sufficient for detection since optically thick clouds at atmospheric temperatures will have more than an order of magnitude higher radiance than background. In the lower troposphere and especially the boundary layer, variable water vapor makes the background continuum radiance more difficult to characterize. We will perform simulations to determine whether seasonal and latitudinal threshold settings are required or whether some of the brightness temperature difference methods, such as used for the nadir data, can also be used for the lowest limb pixels.

Table 8.1: MODIS cloud detection groups*

Detection group	Cloud types	Detection technique(s)	MODIS channels used in detection
I	thick, high clouds (above 500 hPa)	Brightness Temperature (BT) threshold tests for: BT _{13.9} (CO ₂ , 13.9 μ m) BT ₁₁ (window, 11 μ m) BT _{6.7} (H ₂ O, 6.7 μ m)	35 31 27
II	thin, high clouds	BT differences: BT ₁₁ – BT ₁₂ BT _{8.6} – BT ₁₁ BT ₁₁ – BT _{6.7} BT ₁₁ – BT _{3.9}	31, 32 29, 31 31, 27 31, 21
III	low clouds	(daytime) reflectance ratios and BT differences: BT _{3.9} – BT _{3.7}	1, 2, 18 21, 20
IV	thin cirrus	(daytime) reflectance threshold test for 1.38 μ m	26
V	thin cirrus	BT differences: BT _{13.7} – BT _{13.9} BT ₁₁ – BT ₁₂ BT ₁₂ – BT _{3.9}	34, 35 31, 32 32, 21

*Compiled from [Ackerman *et al.*, 1998].

For nadir target data, we plan to adapt the MODIS cloud detection techniques described in [Ackerman *et al.*, 1998]. The Moderate-Resolution Imaging Spectroradiometer (MODIS) will fly on both the EOS Terra (formerly AM) and PM

Table 8.2: MODIS IR bands used for cloud detection and their overlap with TES and AES optical filter bands

MODIS channel	cloud detection group(s)	central wavelength (μm)	frequency range (cm^{-1})	TES filter	AES filter
35	I,V	13.94	710.0 - 725.4	2B1	2B1
34	V	13.64	725.4 - 741.6	2B1	2B1
32	II,V	12.02	815.0 - 849.6	2B1	2B1
31	I,II,V	13.94	886.5 - 927.6	1B1	2B1
29	II	8.55	1149.4 - 1190.5	2A1	1B1,1B2
27	I,II	6.72	1450.3 - 1530.2	2A2*	
21	III	3.96	2506.9 - 2545.2	1A3*	
20	III	3.75	2604.2 - 2732.2	1A4*	

*These filters are not used in the currently defined Global Survey mode.

platforms. MODIS is nadir viewing with 36 channels in the visible and infrared (0.4 to $14.5\ \mu\text{m}$). Table (8.1) summarizes the MODIS cloud detection groups and techniques. Each test within a group produces a confidence level (C.L.) for a cloud free scene and the minimum C.L. is used to represent the group. The C.L. for each group is then used as an indication of the absence of a particular cloud type for generating a cloud mask corresponding to the image data.

Although TES cannot employ the visible and near-IR solar reflection tests used in some of the cloud detection groups, many of the tests involve infrared channels that are within the wavelength range of TES spectra, as seen in Table (8.2). Using TES or AES data, we could easily reproduce the MODIS channels by simply averaging the spectral radiance or brightness temperatures in the MODIS frequency ranges. However, we will also investigate using more specific information in the channels, such as not including spectral lines for bands where window information is desired or selecting only the line centers where CO_2 or H_2O absorption information is being used.

In order to test the utility of these detection techniques with AES data, we selected data taken over the ocean in order to have a background with uniform emissivity. The run first selected was mostly free of clouds (as seen on the video tape recorded simultaneously), but did contain areas of low clouds over which data were collected. Figure (8.1) shows the brightness temperature averaged over

the frequency range for MODIS channel 29 for the 4 AES pixels as a function of scan number (*i.e.*, time). By matching times on the video tape, it was confirmed that scans where the brightness temperatures are below the points clustered near 297K correspond to cloud filled or partially filled pixels. Since AES did not have the information needed for the MODIS method of detecting low clouds, (*i.e.* solar reflection frequency ranges), this data set was not very useful in trying to adapt the MODIS techniques. However, it is apparent from the bottom panel of Figure (8.1) that pixel to pixel variations could provide a reasonable indication of partial cloud filling in the presence of low clouds. Note that although MODIS could also use these types of variations, they are producing an image that includes cloud information while AES and TES (nadir view) will mostly average pixels to produce atmospheric profile information. The pixel to pixel brightness temperature variation is not only a good indication of partially cloudy scenes but also scenes with a large surface variability that could require special processing in Level 2. For TES nadir target data we will compute the largest pixel to pixel brightness temperature variation and flag data where this is above some TBD number (K).

In addition to the cloud tests and pixel-to-pixel variation, TES nadir data will also be flagged when radiance levels are anomalously high and could correspond to biomass fires or volcanic lava. These types of scans would require special level 2 processing.

8.3 Undesired instrument effects

Although we have discussed some of the possible undesired instrumental effects, such as non-linearity, spikes and beamsplitter emission, there are other potential error sources in FTS spectra that will have to be diagnosed and characterized during the TES preflight and commissioning phases. A discussion of other error sources, such as sampling error, both random and periodic is given in [Beer, 1998], along with some of the expected spectral distortions. The pre-launch calibration plan (in preparation) specifies measurements that will detect and characterize such errors and the post-launch calibration and validation plan will describe how to measure and monitor changes from the pre-launch baselines. Algorithms to process these characterization measurements are needed for both detection of errors as well as possible corrections in the data processing.

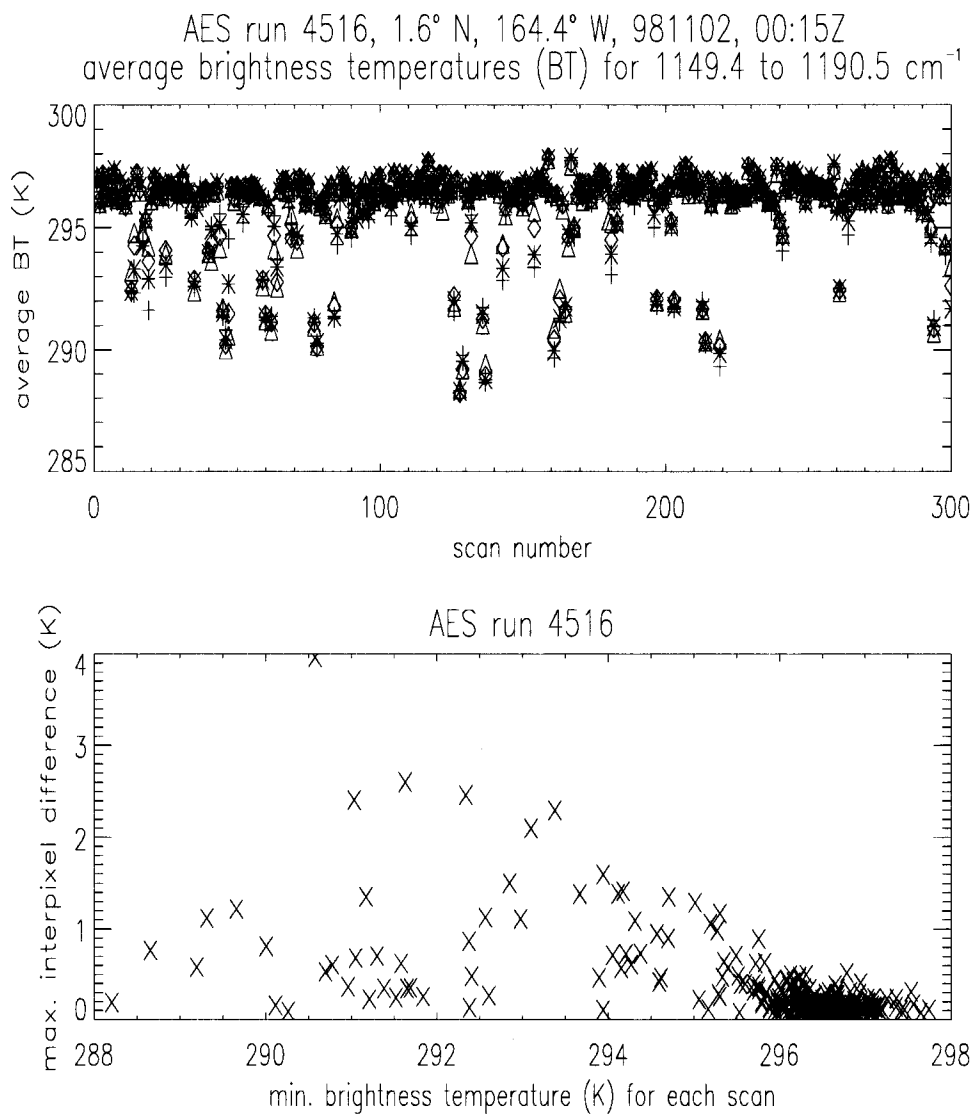


Figure 8.1: Example of AES brightness temperatures corresponding to MODIS channel 29. The different symbols in the top panel represent the 4 AES pixels. Data were taken over the ocean just north of the equator flying SSW. Clouds were thick and low (about 830 mb or 1.5 km, judging from the brightness temperatures and video record), and therefore not detectable with the MODIS techniques using AES data. The bottom panel shows that pixel to pixel brightness temperature variations are a useful criteria for clouds, especially partial cloud filling, in this type of situation.

8.4 Processing errors and data quality history

Processing error flags will always be monitored and their sources investigated, but some may not be of sufficient magnitude or frequency to warrant a halt to the processing of all level 1B data. We give here a preliminary list of such flags:

- 1) The calibrated spectral imaginary has a mean value $>$ TBD.
- 2) The calibrated spectral imaginary RMS is some TBD standard deviations from the RMS of the mean imaginary used to compute the NESR (*i.e.* very noisy spectrum).
- 3) TBD unacceptable spectral calibration error.

APPENDIX A

Broad Band Off-Axis ILS Correction and Modeling

A.1 Filter banks

Filter banks are a means of splitting a signal into frequency subbands. The principle advantage of filter banks over other filtering techniques is that the signal can be reconstructed *perfectly* from its subband components. In fact, filter banks are generally orthogonal or biorthogonal transformations (more on this at the end of the section). In addition to (bi)orthogonality, the computational efficiency of filter banks is comparable to a fast Fourier transform (FFT).

A simple, 2-channel filter bank is shown in Figure (A.1). The filter bank is composed of linear time-invariant (LTI) filters, downsamplers, and upsamplers. A sampled input signal, denoted by $I[n]$, is convolved with the impulse response functions, $h_0[n]$ and $g_0[n]$ ¹. The discrete-time convolution is written as

$$(I * h_0)[n] = \sum_{k \in \mathbb{Z}} I[n - k] h_0[k], \quad (\text{A.1})$$

where $*$ denotes the convolution operation and \mathbb{Z} is the set of integers. The Fourier transform of a convolution operation is converted to an algebraic multiplication. The discrete-time Fourier transform (DTFT) is defined as [Oppenheim

¹The brackets $[\cdot]$ are used to distinguish discrete-time (space) signals from continuous-time (space) signals, which are denoted by (\cdot)

and Schafer, 1989]

$$\hat{I}(\omega) = (\mathcal{F}I)(\omega) = \sum_{k \in \mathbb{Z}} I[k] e^{-ik\omega}, \quad (\text{A.2})$$

where

$$\omega = 2\pi v \Delta x \quad (\text{A.3})$$

is a 2π -normalized, continuous, frequency coordinate and Δx is the sampling period. Note that $\hat{I}(\omega)$ is a *periodic* function of ω with period 2π . Applying the definition of Equation (A.2) to Equation (A.1) leads to

$$\mathcal{F}(I * h_0)(\omega) = \hat{I}(\omega) H_0(\omega), \quad (\text{A.4})$$

where $H_0(\omega)$ is the DTFT of $h_0[n]$. For a 2-channel filter bank, $H_0(\omega)$ allows low-frequency information to pass via Equation (A.4) while suppressing high-frequency information. Thus, $H_0(\omega)$ is the frequency response of a *low-pass* filter. $G_0(\omega)$, which is DTFT of $g_0[n]$, suppresses low-frequency information while allowing high-frequency information to pass. Hence, $G_0(\omega)$ is the frequency response of a *high-pass* filter. The magnitudes of $G_0(\omega)$ and $H_0(\omega)$ are shown in Figure (A.2). The impulse response functions for these filters are listed in Table (A.1).

The phase of these filters, which is shown in Figure (A.3), is linear. The linear phase component of an LTI filter simply delays the input by an amount proportional to the slope of the phase. The linearity of the phase is critical for the ILS correction/modeling problem. The measured interferogram incurs phase dispersion as it traverses the optical and signal chain. This phase dispersion is removed by phase estimation techniques [Forman *et al.*, 1966; Bowman, 1998a]. The phase-corrected interferogram is now symmetric. Since the input into the filter bank is symmetric and the filter has linear phase, the output signals from the analysis bank will also be symmetric. The self-apodization and residual ILS functions, which are also symmetric, can now be directly applied to the subbands.

The filter bank splits an input signal into a low-pass signal and a high-pass signal. These signals are then downsampled. The downsampler operator is defined as [Oppenheim and Schafer, 1989]

$$(\downarrow M I)[n] = I[Mn], \quad (\text{A.5})$$

where M is an integer. The Fourier transform of a downsampled signal is scaled in frequency and includes an aliasing term. The Fourier transform of the signal

that is downsampled by a factor of 2 is

$$(\mathcal{F} \downarrow 2I)(\omega) = \frac{1}{2} \left(\hat{I}\left(\frac{\omega}{2}\right) + \hat{I}\left(\frac{\omega}{2} + \pi\right) \right), \quad (\text{A.6})$$

where $\hat{I}(\omega)$, which is the DTFT of $I[n]$, is periodic in 2π . If the input signal is not sufficiently band-limited, then the downsampling operation will cause aliasing. The filters in Figure (A.1) are designed, however, to insure that this aliasing does not occur.

For a 2-channel filter bank, the filters $h_0[n]$ and $g_0[n]$ reduce the bandwidth of the input signal by a factor of 2. By the Nyquist theorem [Oppenheim and Schaffer, 1989], the filtered signal needs only half as many points. Thus, the downsampler is used after the filter to reduce the total number of points of the filtered signal. For a signal of length N , the low-pass and high-pass output of the filter bank are signals of length $N/2$, respectively. Thus, the total length of the signal is preserved. The filters and downsamplers on the left side of the vertical dash in Figure (A.1) comprise the *analysis* part of the filter bank.

The *synthesis* part of the filter bank, which is on the right side of the vertical dash, is composed of upsamplers and filters. An upsampler is defined as [Oppenheim and Schaffer, 1989]

$$(\uparrow M)I[n] = \begin{cases} I\left[\frac{n}{M}\right] & n = 0, \pm M, \pm 2M, \dots \\ 0 & \text{otherwise.} \end{cases} \quad (\text{A.7})$$

The Fourier transform of a upsampling operation is

$$(\mathcal{F} \uparrow MI)(\omega) = \hat{I}(M\omega). \quad (\text{A.8})$$

The upsampling operator, then, simply scales the DTFT of the input signal.

After the upsampling operation, the low-pass and high-pass signals are then filtered again by $h_1[n]$ and $g_1[n]$, respectively. The output signals of the filtering operation are then recombined.

If h_0 , h_1 , g_0 , and g_1 are chosen carefully, the recombined signal will be the same as the input signal. The filter bank is then said to be a *perfect reconstruction* filter bank. Two conditions must be satisfied for perfect reconstruction to hold [Mallat, 1998]:

$$H_0^*(\omega + \pi)H_1(\omega) + G_0^*(\omega + \pi)G_1(\omega) = 0 \quad (\text{A.9})$$

$$H_0^*(\omega)H_1(\omega) + G_0^*(\omega)G_1(\omega) = 2. \quad (\text{A.10})$$

Equation (A.9) insures that the aliasing is cancelled and Equation (A.10) insures that there is no distortion [Mallat, 1998]. Unfortunately, these conditions do not describe *how* to find suitable filters. The problem may be simplified by adding these constraints:

$$G_1(\omega) = -H_0(\omega + \pi) \quad (\text{A.11})$$

$$G_0(\omega) = H_1(\omega + \pi). \quad (\text{A.12})$$

In the time domain, these relations become

$$g_0[n] = (-1)^n h_1[n] \quad (\text{A.13})$$

$$g_1[n] = -(-1)^n h_0[n]. \quad (\text{A.14})$$

An additional constraint on these filters is that their impulse responses must be finite. Naturally, this class of filters is called finite impulse response (FIR) filters. The restriction to FIR filters is essential because they are computationally efficient. In addition, it is generally easier to design FIR filters that satisfy the conditions of Equations (A.9) and (A.10) than other kinds of filters.

It should be pointed out that Figure (A.1) shows the filter bank at a conceptual level. Filter banks are *not* implemented as filters followed by downsamplers. Instead, the input signal is separated into even and odd components. When this is done, the downsamplers in the analysis bank can be interchanged with the filters. Restructuring the filter bank in this way is known as a *polyphase* implementation [Strang and Nyugen, 1996]. This form of the filter bank is very efficient. For FIR filters with filter coefficients of length L and an input signal of length N ,

$$\text{operations needed to generate output of analysis bank} < 2LN. \quad (\text{A.15})$$

An FFT, on the other hand, requires $O(N \log N)$ multiplications². Thus, for filters with a small number of coefficients, filter banks can actually be computed faster than an FFT.

A considerable amount of research has been done on designing filters that satisfy the above properties [Mallat, 1998; Strang and Nyugen, 1996]. We will restrict my attention to biorthogonal linear-phase filter banks. The term biorthogonal refers to the basis set that is implied by the filter bank. The analysis part of the filter bank can be described by a matrix operation. If the input signal is assembled into a vector $\mathbf{x} \in \mathbb{R}^N$, then the output signal of the analysis bank is

$$\mathbf{y} = \mathbf{A}\mathbf{x}, \quad (\text{A.16})$$

² O means "on the order of"

where $\mathbf{y} \in \mathbb{R}^N$ and $\mathbf{A} \in \mathbb{R}^{N \times N}$ is the matrix that represents the analysis bank. Likewise, the synthesis bank can be represented as

$$\mathbf{x} = \mathbf{S}^\top \mathbf{y}, \quad (\text{A.17})$$

where $\mathbf{S} \in \mathbb{R}^{N \times N}$ is the matrix that represents the synthesis bank. From Equations (A.16) and (A.17) it follows that

$$\mathbf{S}^\top \mathbf{A} = \mathbf{I}, \quad (\text{A.18})$$

where \mathbf{I} is the identity matrix. Equation (A.18) is the matrix representation of the biorthogonality condition. For certain kinds of filter, $\mathbf{A} = \mathbf{S}$. In this case, the matrices in Equation (A.18) are unitary and the transformation is orthogonal. Filter banks have analogues in continuous-time; these analogues are called wavelet packets [Mallat, 1998]. Since we do not exploit the continuous-time property, this aspect of filter banks is not emphasized.

The properties of the 2-channel case can be easily extended to higher channels. Figure (A.4) shows the analysis part of a 4-channel filter bank. The low-pass and high-pass components of the first stage are split again into smaller frequency bands. Since each stage of the analysis bank can be perfectly reconstructed from the same stage in the synthesis bank, the entire filter bank maintains the perfect reconstruction property. In addition to iterating the 2-channel case, there are also M-channel filter banks and lapped orthogonal transforms (LOT) that could also be used [Strang and Nyugen, 1996].

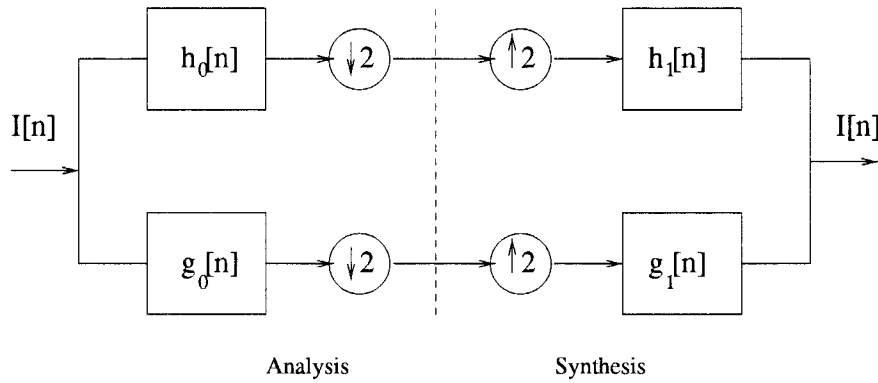


Figure A.1: 2-channel filter bank

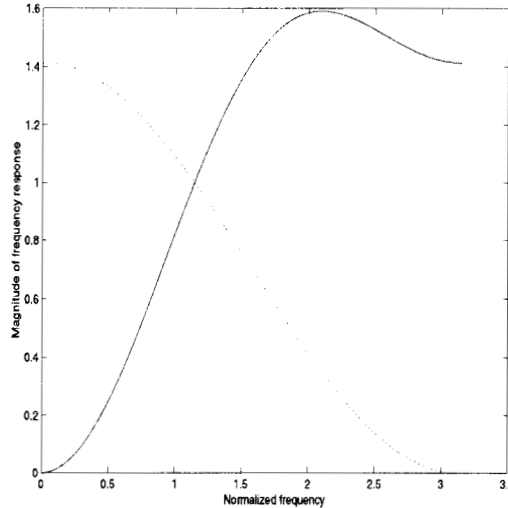


Figure A.2: Frequency response of the biorthogonal filters. The low-pass frequency response is $H_0(\omega)$ and the high-pass frequency response is $G_0(\omega)$.

A.2 Off-axis ILS algorithm for the 2-channel case

As described in Section (6.3), the off-axis ILS correction/modeling algorithm must be split between Level 1B and Level 2. Figure (A.5) shows the processing steps for Level 1B. For simplicity, we will consider the 2-channel case. The approach can be extended to a greater number of channels in a straight-forward manner. First, the spectrum is radiometrically calibrated. Then, the measured interferogram is split into two interferograms that represent the low-pass and high-pass parts of the spectrum, respectively. Thus, these two interferograms, $I_1[n]$ and $I_2[n]$, correspond to the frequency bands in Equation (6.12). The self-apodization term in Equation (6.10) is divided out from both interferograms and then recombined into two interferograms. Finally, the interferogram is resampled at the rate of the scale factor. The Level 1B output interferogram $I_{L1B}[n]$ still has the residual ILS terms, which must be removed in Level 2.

Figure (A.6) shows the processing steps for Level 2. The forward model interferogram, $I_F[n]$, is split into a low-pass interferogram $I_{F,1}[n]$ and a high-pass interferogram $I_{F,2}[n]$. Each interferogram is then multiplied by a residual ILS function evaluated at $\bar{\nu}_1$ and $\bar{\nu}_2$, respectively. The resulting interferograms are then recombined to produce $I_{L2}[n]$. Ideally, the difference between $I_{L2}[n]$ and $I_{L1B}[n]$ is

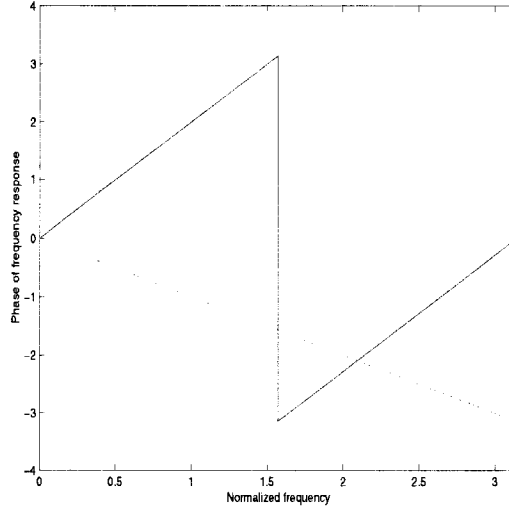


Figure A.3: Phase of the frequency response of the biorthogonal filters.

negligible.

This technique was tested for a simulated limb spectrum over a spectral region between $1040 - 1060 \text{ cm}^{-1}$. An off-axis interferogram was modeled using Equation (6.5) for the 8th off-axis detector element; the physical model, including the pixel response function, is discussed in [Worden and Bowman, 1998]. The Fresnel kernel was calculated for $\bar{\nu}_1 = 1045 \text{ cm}^{-1}$ and $\bar{\nu}_2 = 1055 \text{ cm}^{-1}$. The compression factor for both Fresnel kernels was $\rho = 1.818 \times 10^{-5}$. The magnitudes of the Fresnel kernels and their non-linear phases are shown in Figures (A.7) and (A.8). The filter bank coefficients that were used are shown in Table (A.1). The coefficients for $g_0[n]$ and $g_1[n]$ can be found by applying the relations in Equations (A.13) and (A.14). Note that we have only listed half of the coefficients for each filter. These filters are symmetric about the first elements in Table (A.1). For example, $\{h_0\} = \{\dots, .767245, .383269, .767245, \dots\}$. The spectrum produced from Level 1B processing for this case is shown in Figure (A.9). The error between the on-axis spectrum and the Level 1B corrected spectrum is defined as

$$\epsilon = \frac{\max(|F_{on-axis}(\omega) - F_{L1B}(\omega)|)}{\text{mean}(F_{on-axis}(\omega))}. \quad (\text{A.19})$$

In this case, $\epsilon_{1B-only} = .00289$, which is roughly a .3% error. The on-axis interferogram is now multiplied by the residual ILS functions via the filter banks in

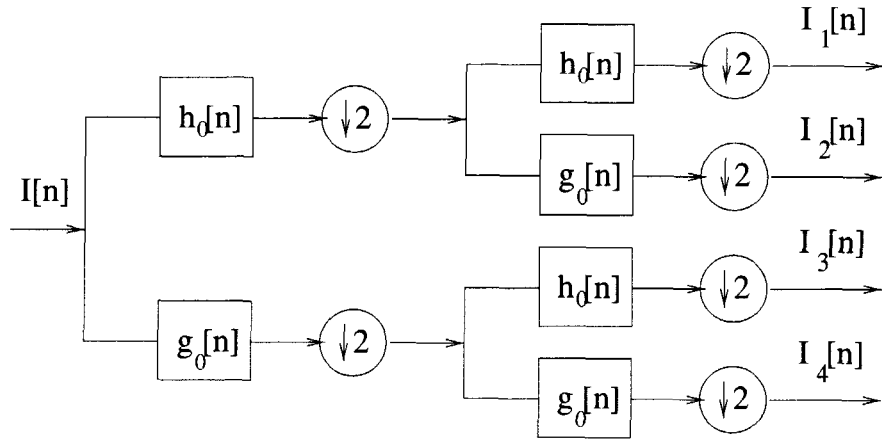


Figure A.4: 4-channel filter bank based on iterating the 2-channel case. Only the analysis bank is shown. The synthesis bank is simply the reverse of the analysis bank where the downsamplers are replaced by upsamplers.

Figure (A.6). The resulting spectrum is compared to the output of the Level 1B processing, which is shown in Figure (A.10). The error between the Level 1B processing and Level 2 is now $\epsilon_{combined} = .000519$, which is over a factor of 5 improvement than just doing the Level 1B processing alone. Moreover, this systematic error, which is around .05% is quite acceptable compared to the estimated measurement error of .36% for the 1B2 filter in the tropics [Beer, 1996].

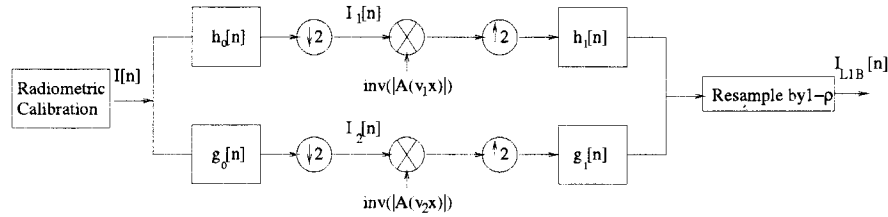


Figure A.5: Level 1B processing: The functions $h_0[n]$ and $h_1[n]$ refer to low-pass filters while $g_0[n]$ and $g_1[n]$ refer to high-pass filters. The uparrows and downarrows refer to upsampling and downsampling, respectively.

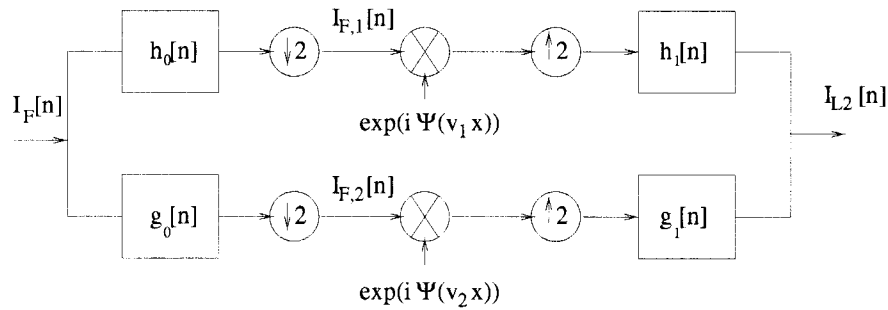


Figure A.6: Level 2 processing

Table A.1: Filter bank coefficients

h_0	.383269
	.767245
	.383269
	-.068867
	-.033475
	.047282
	.003759
	-.008473
h_1	.832848
	.448109
	-.069163
	-.108737
	.006292
	.014182

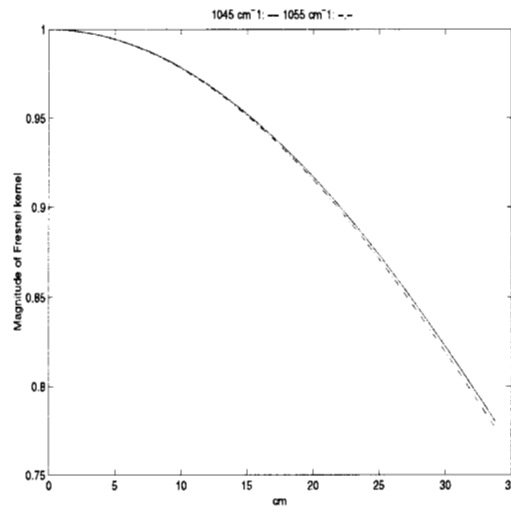


Figure A.7: Magnitude of the Fresnel kernel, which is also called the self-apodization function, for 1045 and 1055 cm⁻¹.

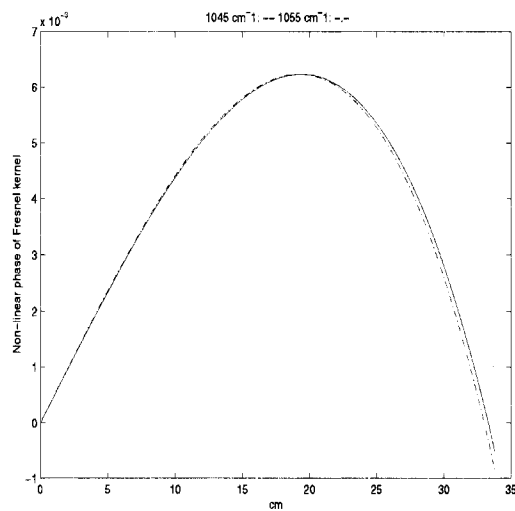


Figure A.8: Residual Fresnel phase function for 1045 and 1055 cm^{-1} . The complex exponent of these functions are the residual ILS functions.

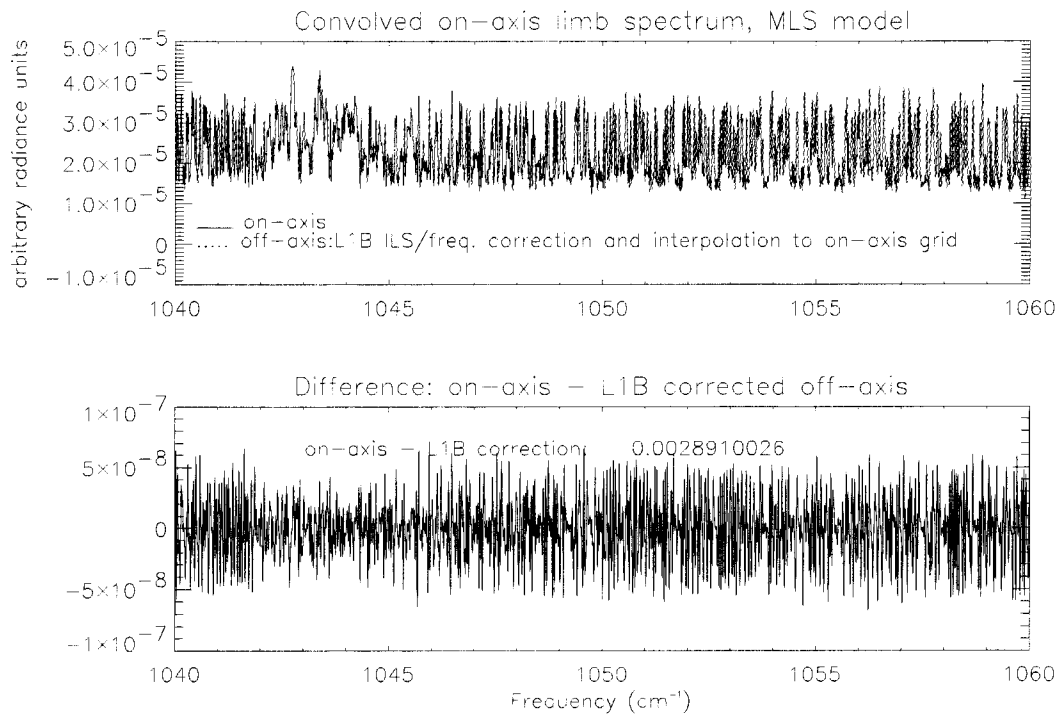


Figure A.9: Comparison between on-axis spectrum and the off-axis spectrum after Level 1B correction.

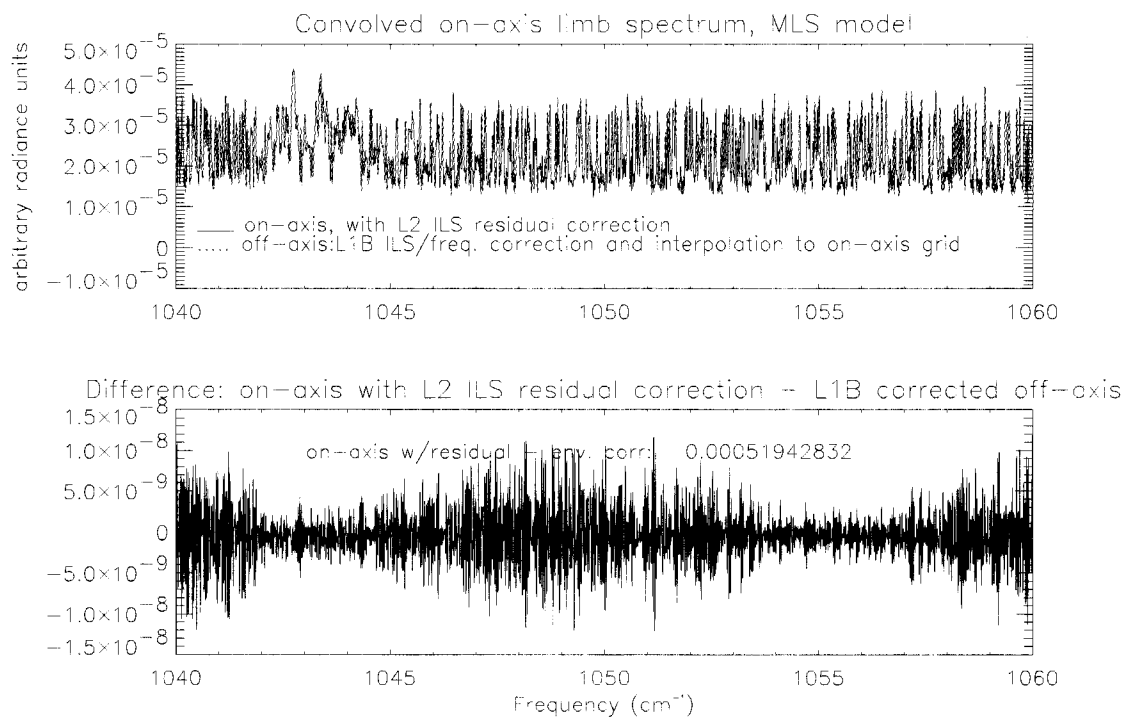


Figure A.10: Comparison between the on-axis spectrum with the residual ILS functions and the off-axis spectrum after Level 1B correction.

APPENDIX B

Optional Phase Correction Techniques

B.1 Introduction

In a practical FTS, input radiation passes through dispersive elements in the optical system and electronics. For TES, the zero path difference (ZPD) of the interferogram is unlikely to be sampled. The result of these instrumental effects is a measured interferogram that is asymmetric, which leads to a spectrum that is complex. Furthermore, the instrument may introduce negative amplitudes in the radiance and will therefore cause π shifts in the phase of the spectrum. These negative amplitudes can occur when differencing the target radiance with an internal radiance—such as a cold reference plate—that results in a negative signal. The phase correction problem is the estimation and removal of the phase due to the non-ZPD sampling and dispersion while preserving the negative amplitudes of the spectrum. Naturally, this estimation must be performed in the presence of noise.

A complex spectrum measured from a double-sided FTS is modeled as

$$L_m(\nu) = L(\nu)e^{i\phi(\nu)} + n(\nu), \quad (\text{B.1})$$

where $L_m(\nu)$ is the measured spectrum, $L(\nu)$ is the input spectrum, $n(\nu)$ is additive white noise, and $\phi(\nu)$ is the phase due to non-ZPD sampling and dispersion. This phase may be expressed as the

$$\phi(\nu) = 2\pi\alpha\nu + \phi_{NL}(\nu). \quad (\text{B.2})$$

The dominant component of the linear term in Equation (B.2) results from not sampling the ZPD and is thus called the *sampling phase*. The other contribution to the linear term comes from the dispersion. The non-linear term, denoted as ϕ_{NL} results strictly from dispersion in the instrument and is therefore called the *dispersion phase*. The sum is called the *sampling/dispersion phase*.

Phase correction is performed by multiplying Equation (B.1) by an estimate of the instrument phase function. The phase corrected spectrum is

$$\hat{L}(v) = L_m(v) e^{-i\hat{\phi}(v)} \quad (\text{B.3})$$

$$= L(v) e^{i(\phi(v) - \hat{\phi}(v))} + n(v) e^{-i\hat{\phi}(v)}, \quad (\text{B.4})$$

where $\hat{L}(v)$ is the phase corrected spectrum and $\hat{\phi}$ is an estimate of the sampling/dispersion phase function. If an exact estimate of the sampling/dispersion phase function were computed, i.e. $\hat{\phi} = \phi$, then the imaginary and real components of the phase corrected spectrum would be

$$\text{Im}\{\hat{L}(v)\} = \text{Im}\{n(v)\} \sin(\hat{\phi}(v)) \quad (\text{B.5})$$

$$\text{Re}\{\hat{L}(v)\} = L(v) + \text{Re}\{n(v)\} \cos(\hat{\phi}(v)), \quad (\text{B.6})$$

where $\text{Re}\{\cdot\}$ and $\text{Im}\{\cdot\}$ are the real and imaginary components of a function. Thus, for a perfect phase estimate, the imaginary component of the spectrum approximates white noise. The real component of the spectrum is now simply the input spectrum with additive noise. In this sense, the spectrum has been “rotated” into the real component. Nevertheless, even for a perfect estimate, there will always be some redistribution of the noise between the real and imaginary components of the spectrum because of the phase correction process.

There are two techniques that might be used for phase correction of spectra at higher frequencies: the Forman-Vanesse-Steel (FVS) and the optimal phase estimator (OPE). Both techniques correct the individual spectrum and do not need the calibration spectra. Moreover, they are insensitive to changes in the non-linear component of the phase function. On the other hand, they can not be used when beam splitter emission is significant relative to the input spectrum. Nevertheless, for frequencies above 1200 cm^{-1} , this emission term is small. Thus, these techniques could be considered in this frequency regime. In addition, these techniques can be used for nadir viewing since the input spectrum is much larger than the self-emission from the beam splitter. However, the FVS technique can not be applied to limb spectra because of π shifts in the phase function due to oscillations about zero [Bowman, 1998b].

B.2 Optimal phase estimator

For the optimal phase estimator, the phase function must be parameterized, so

$$\phi(\mathbf{v}) \mapsto \phi(\mathbf{v}; \mathbf{x}), \quad (\text{B.7})$$

where $\mathbf{x} \in \mathbb{R}^P$ is the parameter state vector. The elements of this state vector are coefficients of an expansion on a basis set described by

$$\phi(\mathbf{v}) \approx \sum_{m=1}^P x_m \Phi_m(\mathbf{v}), \quad (\text{B.8})$$

where $x_m = [\mathbf{x}]_m$. Naturally, any number of bases can be chosen such as polynomials, splines, wavelets, SVD, etc. This choice is independent of the derivation of the optimal phase estimator. For the examples to follow, however, a simple second-order polynomial was used. Thus,

$$\Phi_m(\mathbf{v}) = \mathbf{v}^{m-1}, \quad (\text{B.9})$$

where $m = 1, 2, 3$.

In order to proceed, the corrected spectrum must be converted into vector notation. Let $\hat{\mathbf{F}}(\mathbf{x}) \in \mathbb{C}^N$, where N is the number of spectral points, be the corrected spectrum whose elements are defined by

$$[\hat{\mathbf{F}}(\mathbf{x})]_j = L_m(\mathbf{v}_j) e^{-i\hat{\phi}(\mathbf{v}_j; \mathbf{x})}, \quad (\text{B.10})$$

where \mathbf{v}_j is the j^{th} spectral point. The *residual* of the corrected spectrum is defined by

$$\mathbf{r}(\mathbf{x}) = \text{Im}(\hat{\mathbf{F}}(\mathbf{x})), \quad (\text{B.11})$$

where $\mathbf{r}(\mathbf{x}) \in \mathbb{R}^N$. The problem is now to minimize the vector normed error function

$$f(\mathbf{x}) = \frac{1}{2} \|\mathbf{r}(\mathbf{x})\|^2 \quad (\text{B.12})$$

with respect to the state vector \mathbf{x} . In order to minimize Equation (B.12), the *Jacobian* is defined as

$$[\mathbf{K}(\mathbf{x})]_{i,j} = \frac{\partial r_i(\mathbf{x})}{\partial x_j} \quad (\text{B.13})$$

for $\mathbf{r}(\mathbf{x})$ where $\mathbf{K}(\mathbf{x}) \in \mathbb{R}^{N \times P}$. The variables $r_i(\mathbf{x})$ and x_j are the i^{th} and j^{th} elements of $\mathbf{r}(\mathbf{x})$ and \mathbf{x} , respectively. A solution of Equation (B.12) is the *Gauss-Newton* method [Björck, 1996]

$$\mathbf{x}_{i+1} = \mathbf{x}_i - [\mathbf{K}^\top(\mathbf{x}_i)\mathbf{K}(\mathbf{x}_i)]^{-1}\mathbf{K}^\top(\mathbf{x}_i)\mathbf{r}(\mathbf{x}_i). \quad (\text{B.14})$$

This equation is called the *optimal phase estimator*.

The complete OPE algorithm can be described in the following steps:

1. Align the sampling phase (Equation (5.6)) to the 340K blackbody spectrum.
2. Estimate the parameterized phase function of the blackbody starting at an arbitrary initial guess, such as $\mathbf{x} = \mathbf{0}$.
3. Align the sampling phase of the target spectrum (Equation (5.5)).
4. Estimate the phase function of the target spectrum starting with the estimate of the black body phase function as an initial guess.
5. Correct target spectrum with estimated target phase function.

For more details of the validation of this algorithm, see [Bowman, 1998b].

B.3 FVS phase estimation

The FVS method [Forman et al., 1966] for estimating the phase is based on calculating a smoothed version of the spectrum from a kernel of the interferogram. There are two assumptions that undergird this method:

- the phase function is smooth,
- the interferogram is a broad-band signal.

The latter assumption means that most of the energy of the interferogram is concentrated around zero path difference (ZPD). A measured interferogram is described by

$$I(x) = I_F(x) + n(x), \quad (\text{B.15})$$

where $I_F(x)$ is the interferogram associated with the input spectrum and $n(x)$ is Gaussian, white noise. Most of the energy in an interferogram is generally concentrated around the ZPD while the noise is distributed evenly. A good estimate

of the input spectrum can be calculated by multiplying the interferogram with a box of width, say, 2 cm centered around zero index. Most of the energy in the interferogram will be preserved while the noise will be severely attenuated. The estimated spectrum is then

$$\hat{L}(v) = \int_{-\infty}^{\infty} p_l(x) I(x) e^{-i2\pi vx} dx, \quad (\text{B.16})$$

where

$$p(x) = \begin{cases} 1, & |x| < l/2 \\ 0, & \text{otherwise} \end{cases} \quad (\text{B.17})$$

is the box function. Equation (B.16) can be interpreted as a low-pass filtering operation that generates a smoothed version of $L(v)$. In the spectral domain, Equation (B.16) is written as a convolution operation

$$\hat{L}(v) = \int_{-\infty}^{\infty} P(\tau) L_m(v - \tau) d\tau, \quad (\text{B.18})$$

where $L_m(v)$ is the Fourier transform of $I(x)$ and

$$P(v) = \frac{\sin 2\pi l v}{\pi v} \quad (\text{B.19})$$

is the Fourier transform of $p(x)$. The smoothed estimate of $L(v)$ is now used to calculate a smoothed estimate of the phase through the relation

$$\hat{\phi}(v) = \arctan \frac{\text{Im}(\hat{L}(v))}{\text{Re}(\hat{L}(v))}. \quad (\text{B.20})$$

In practice, the functions are sampled and thus discrete signals are processed. In practice, the phase function estimate in Equation (B.20) is calculated only over the width of the box, $p(x)$. The interferogram of the phase estimate is then

$$I_{\hat{\phi}}(x) p_l(x) = \frac{1}{2\pi} \int_{-\infty}^{\infty} e^{i\hat{\phi}(v)} e^{i2\pi vx} dv. \quad (\text{B.21})$$

Thus, the interferogram is non-zero only over the box. If this interferogram is simply zero-padded and its Fourier transform recalculated over the width of the scan, then there will be excessive numerical ringing in the resulting spectrum. In

order to avoid this ringing, an apodization is applied to the interferogram of the form [Filler, 1964]

$$a(x) = \frac{1}{2}(\cos(x) + \frac{1}{5} \cos(3x)). \quad (\text{B.22})$$

The phaser associated with the phase estimate is then

$$e^{i\hat{\phi}_a(v)} = \int_{-\infty}^{\infty} a(x) p_l(x) I_{\hat{\phi}}(x) e^{-i2\pi vx} dx. \quad (\text{B.23})$$

The phase estimate calculated in Equation (B.23) is then used to correct the spectrum via Equation (B.3).

Bibliography

- Ackerman, S., K. Strabala, W. Menzel, R. Frey, C. Moeller, and L. Gumley, Discriminating clear sky from clouds with modis, *J. Geophys. Res.*, *103*, 32,141–32,157, 1998.
- Beer, R., *Remote Sensing by Fourier Transform Spectrometry*, John Wiley & Sons, New York, London, Sydney, 1992.
- Beer, R., Tropospheric Emissions Spectrometer: scientific objectives and approach, goals and requirements, *D-11294*, JPL, 1996, revision 5.0.
- Beer, R., Peak-finding algorithms, *TES A/S-DFM 43*, JPL, 1997.
- Beer, R., A compendium of horrors, *TES A/S-DFM 60*, JPL, 1998.
- Beer, R., Tropospheric Emissions Spectrometer: scientific objectives and approach, goals and requirements, *D-11294*, JPL Internal Document, 1999, revision 6.0.
- Beer, R., T. Glavich, and D. Rider, Tropospheric Emission Spectrometer (TES) for the Earth Observing System (EOS) chemistry I satellite: I objectives, requirements and instrument overview, *Applied Optics*, 1999, submitted for publication.
- Bell, R., *Introductory Fourier Transform Spectroscopy*, Academic Press, New York, 1972.
- Björck, Å., *Numerical Methods for Least Squares Problems*, SIAM Publ., 1996.
- Blom, C., M. Höpfner, and C. Weddigen, Correction of phase anomalies of atmospheric emission spectra by the double-differencing method, *Applied Optics*, *35*, 4586–4589, 1996.

- Bowman, K., Off-axis modeling and correction, *TES-DFM 286-V*, JPL, 1997.
- Bowman, K., A Bayesian approach to phase correction, *TES A/S-DFM 56*, JPL, 1998a.
- Bowman, K., Optimal phase estimation for a Fourier transform spectrometer, *TES A/S-DFM 77*, JPL, 1998b.
- Bowman, K., H. Worden, and R. Beer, Instrument line shape modeling and correction for off-axis detectors in Fourier transform spectrometry, *Applied Optics*, 1999, submitted for publication.
- Cameron, D., J. Kauppinen, D. Moffatt, and H. Mantsch, Precision in condensed phase vibrational spectroscopy, *Appl. Spectrosc.*, **36**, 245, 1982.
- Filler, A., Apodization and interpolation in Fourier transform spectroscopy, *J. Opt. Soc. Am. A.*, **54**, 762, 1964.
- Forman, M. L., W.H.Steel, and G. Vanasse, Correction of asymmetric interferograms obtained in Fourier spectroscopy, *J. Opt. Soc. Am. A.*, **56**, 59, 1966.
- Frigo, M., and S. Johnson, Adaptive software architecture for the FFT, in *IEEE International Conference on Acoustics, Speech, and Signal Processing*, vol. 3, pp. 1381–1384, 1998.
- Goodman, J. W., *Statistical Optics*, John Wiley & Sons, New York, London, Sydney, 1985.
- Holm, R., Instrument calibration plan, *D-13432*, JPL Internal Document, 1999.
- Jansson, P., *Deconvolution With Applications in Spectroscopy*, Academic Press, 1984.
- Lachance, R., Envisat-1 ground segment MIPAS ATBD for level 1b processing, *PO-TN-BOM-GS 0012*, BOMEM, 1998.
- Loan, C. V., *Computational Frameworks for the Fast Fourier Transform*, SIAM Publ., 1992.
- Mallat, S., *A Wavelet Tour of Signal Processing*, Academic Press, New York, 1998.

- Oppenheim, A. V., and R. W. Schaffer, *Discrete-Time Signal Processing*, Prentice-Hall, Englewood Cliffs, N.J., 1989.
- Revercomb, H., H. Buijs, H. Howell, D. Laporte, W. Smith, and L. Stromovsky, Radiometric calibration of IR Fourier transform spectrometers: solution to a problem with the high-resolution interferometer sounder, *Applied Optics*, 27, 3210–3218, 1988.
- Strang, G., and T. Nyugen, *Wavelets and Filter Banks*, Wellesley-Cambridge Press, Wellesley, 1996.
- Weddigen, C., C. Blom, and M. Höpfner, Phase corrections for the emission sounder MIPAS-FT, *Applied Optics*, 32, 4586–4589, 1993.
- Worden, H., and K. Bowman, Validation of correction for off-axis ILS, *TES-DFM 439-V*, JPL, 1998.
- Worden, H., R. Beer, and C. Rinsland, Airborne infrared spectroscopy of 1994 western wildfires, *J. Geophys. Res.*, 102, 1287–1299, 1997.

APPENDIX C

Instrument Description

Tropospheric Emission Spectrometer (TES) for the Earth Observing System (EOS) CHEMISTRY I Satellite. I: Objectives, Requirements & Instrument Overview

Reinhard Beer, Thomas A. Glavich and David M. Rider

Jet Propulsion Laboratory
California Institute of Technology
Pasadena, CA

Abstract

The Tropospheric Emission Spectrometer (TES) is an imaging infrared Fourier transform spectrometer scheduled to be launched into polar sun-synchronous orbit on the Earth Observing System (EOS) CHEMISTRY 1 satellite in December 2002. We describe how the overall mission objectives flow down to the specific science and measurement requirements and how, in turn, these are implemented in the flight hardware.

Keywords: Atmospheric composition; Ozone; Remote sensing; Spectrometers and spectroscopic instrumentation; Spectroscopy, Fourier transforms

Introduction

The EOS CHEMISTRY I Mission

In January 1988, NASA invited proposals for participation in a new program of polar Sun-synchronous orbiting platforms to be called the Earth Observing System (EOS). The objectives of this program have been stated in a variety of forms but most succinctly as a series of questions.¹

- 1) What are the nature and extent of land-cover and land-use change and the consequences for sustained productivity?*
- 2) How can we enable regionally useful forecasts of precipitation and temperature on seasonal-to-interannual time frames?*
- 3) Can we learn to predict natural hazards and mitigate natural disasters?*
- 4) What are the causes and impacts of long-term climate variability and can we distinguish natural from human-induced drivers?*
- 5) How and why are concentrations and distributions of atmospheric ozone changing?*

The Tropospheric Emission Spectrometer (TES) was successfully proposed for this mission, the particular emphasis being on Question 5 but with some useful input into Questions 2, 3 & 4.

After a number of program reviews and restructurings, the spaceborne part of the mission was divided into 3 parts: a largely Earth-surface orientated platform called "AM-1" (recently re-named "TERRA"); a second platform, called "PM-1", to concentrate on climate and a third one called "CHEMISTRY 1" for the chemistry of the troposphere and lower stratosphere. TES was assigned to this latter platform as were three other instruments - the Microwave Limb Sounder (MLS), the High Resolution Dynamics Limb Sounder (HiRDLS) and the Ozone Measuring Instrument (OMI). The CHEMISTRY 1 satellite will be launched in December 2002 into a Sun-synchronous orbit with a nominal 1:45 p.m. equator crossing time (Fig. 1). The orbit repeats exactly every 16 days (= 233 orbits) with a near-repeat every 2 days.

Fig. 1: CHEM Platform in color (updated to show OMI!)

The Troposphere

The *troposphere* is the region of the Earth's lower atmosphere that is dominated by convective processes. It extends from the surface, with declining temperature, up to the boundary with the stratosphere (the *tropopause*). The height of the tropopause varies with latitude and season, generally being highest in the tropics and lowest at the poles. An average thermal structure of the atmosphere is shown in Fig.2.

The troposphere is, in turn, often sub-divided into vertical zones. The lowest 1-2 km is termed the *boundary layer*, a region of strong horizontal and vertical mixing. Above this is the *free troposphere* where much of the important photochemistry occurs. At the top is the *upper troposphere* wherein transport to and from the stratosphere becomes important.

TES-Specific Objectives

The primary objective of TES is to map the global 3-dimensional distribution of tropospheric ozone (O_3) and the chemical species involved in its formation and destruction (so-called "precursors"). This is a very ambitious objective because a) only about 10% of the total ozone in the Earth's atmosphere is in the troposphere - most is in the stratosphere through which, of course, any spaceborne system must observe, and b) many of the critical precursors exist only at very low concentrations (fractions of a part-per-billion by volume, ppbv). It therefore requires a very carefully designed, high performance, instrument to make the necessary measurements. In particular, such low concentrations can generally only be measured by the technique of limb sounding (a sideways view through the atmosphere), which increases the path length some 100-fold at the expense of poorer spatial resolution along the line of sight.

On the other hand, the major species such as ozone itself, water vapor, carbon monoxide and methane are readily measured by nadir viewing (with better localization but relatively limited vertical resolution), so an initial requirement on TES is that it must provide both limb and nadir sounding capability.

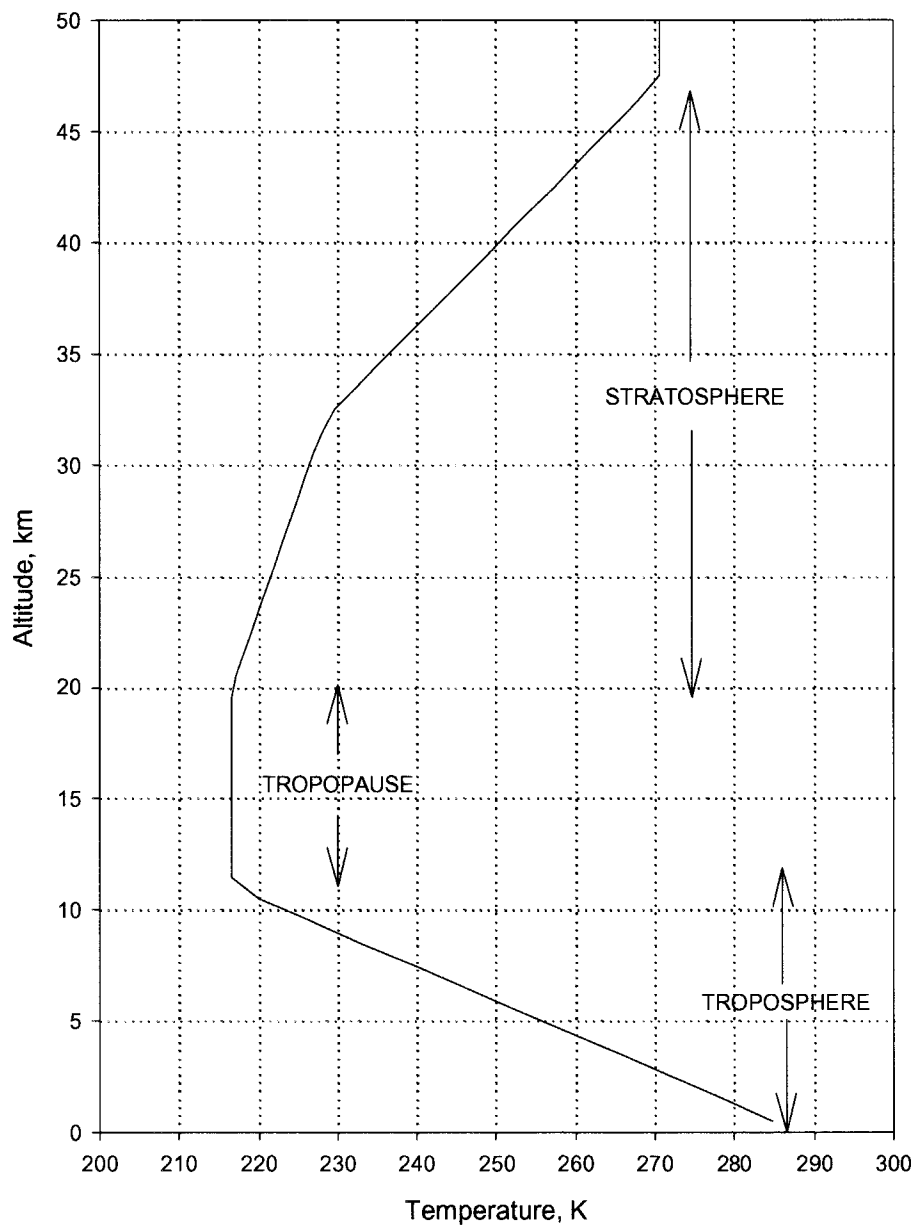


Fig. 2: The 1976 US Standard Atmosphere Temperature Profile. Zones important to TES are indicated

Tropospheric Ozone

Ozone is produced in the troposphere by photochemical oxidation of carbon monoxide (CO) and hydrocarbons in the presence of nitrogen oxides (NO_x) and water vapor (H₂O). These ozone precursors have both natural and anthropogenic sources. The chemistry of ozone is complex and tightly coupled to the atmospheric transport of both ozone and its precursors.

Tropospheric ozone has three major environmental impacts:

- 1) *As an air pollutant.* Ozone in surface air is toxic to humans, animals and vegetation. It is the principal harmful component of smog.
- 2) *As a cleansing agent.* Photolysis of ozone in the presence of water vapor is the primary source of the hydroxyl radical (OH), which is the main oxidant in the atmosphere. Reactions with OH in the lower and middle troposphere are the principal sink for a large number of environmentally-important species including air pollutants (carbon monoxide), greenhouse gases (methane), and gases depleting the stratospheric ozone layer (HCFC's, methyl halides).
- 3) *As a greenhouse gas.* Ozone in the middle and upper troposphere is an efficient greenhouse gas. Perturbation of ozone in this region of the atmosphere results in heterogeneous radiative forcing with complicated implications for climate.

The environmental implications of tropospheric ozone are therefore very different from those of stratospheric ozone. The ozone layer in the stratosphere shields the Earth's surface from solar UV-B radiation, and thinning of this layer as a result of human activities is a matter of grave concern. Tropospheric ozone, by contrast, has increased as a consequence of human activity (primarily because of combustion processes). Whether this increase in tropospheric ozone is beneficial (cleansing agent) or harmful (air pollutant, greenhouse gas) depends to a large extent on its altitude. It is very important, therefore, to map the global 3-dimensional distribution of tropospheric ozone and its precursors in order to improve our understanding of the factors controlling ozone in different regions of the troposphere.

TES Data Products

In the EOS program, data products are divided into 2 classes: Standard Products, which are produced routinely and archived in a publically-accessible location, and Special Products, which have more of a research nature and are produced on an "on demand" and non-interference basis.

The Standard Products that TES will produce are global-scale vertical concentration profiles (0 - ~35 km) of ozone, water vapor, carbon monoxide, methane, nitric oxide, nitrogen dioxide and nitric acid (the latter 3 in the mid- and upper troposphere only) every 4 days out of 8. Essential by-products of the analysis are atmospheric temperature profiles and surface temperature and emissivity. Table I lists the Standard Products and Table II is a partial list of potential Special Products. In both cases, an indication of the necessary observation conditions is shown.

Table I: TES Standard Products & Required Sensitivity

Product Name	Product Source		Required Sensitivity*
	Nadir	Limb	
Level 1A Interferograms	✓	✓	
Level 1B Spectral Radiances	✓	✓	
Atmospheric Temperature Profile	✓	✓	0.5 K
Surface Skin Temperature	✓		0.5 K
Land Surface Emissivity [†]	✓		0.01
Ozone (O ₃) VMR Profile	✓	✓	1 - 20 ppbv
Water Vapor (H ₂ O) VMR Profile	✓	✓	1 - 200 ppmv
Carbon Monoxide (CO) VMR Profile	✓	✓	3 - 6 ppbv
Methane (CH ₄) VMR Profile	✓	✓	14 ppbv
Nitric Oxide (NO) VMR Profile		✓	40 - 80 pptv
Nitrogen Dioxide (NO ₂) VMR Profile		✓	15 - 25 pptv
Nitric Acid (HNO ₃) VMR Profile		✓	1 - 10 pptv
Nitrous Oxide (N ₂ O) VMR profile	✓	✓	Control [‡]

* Sensitivity range maps to expected concentration range (higher concentration → higher uncertainty)

[†] Water (and, probably, snow & ice) emissivity is known and are therefore *input*, not output parameters

[‡] Tropospheric concentration known

Table II: Potential Special (Research) Products

Chemical Group	Common Name	Formula	Product Source	
			Nadir	Limb
H_xO_y	Hydrogen Peroxide	H ₂ O ₂		✓
	Monodeuterated Water Vapor	HDO	✓	✓
C-compounds	Ethane	C ₂ H ₆		✓
	Acetylene	C ₂ H ₂		✓
	Formic Acid	HCOOH	✓	✓
	Methyl Alcohol	CH ₃ OH	✓	✓
	Peroxyacetyl Nitrate	CH ₃ C(O)NO ₂		✓
	Acetone	CH ₃ C(O)CH ₃		✓
	Ethylene	C ₂ H ₄		✓
N-compounds	Peroxynitric Acid	HO ₂ NO ₂		✓
	Ammonia	NH ₃	✓*	✓
	Hydrogen Cyanide	HCN		✓
	Dinitrogen Pentoxide	N ₂ O ₅		✓
Halogen compounds	Hydrogen Chloride	HCl	✓*	
	Chlorine Nitrate	ClONO ₂		✓
	Carbon Tetrachloride	CCl ₄		✓
	CFC-11	CCl ₃ F	✓	✓
	CFC-12	CCl ₂ F ₂	✓	✓
	HCFC-21	CHCl ₂ F		✓
	HCFC-22	CHClF ₂		✓
S-compounds	Sulfur Dioxide	SO ₂	✓	✓
	Carbonyl Sulfide	OCS	✓	✓
	Hydrogen Sulfide	H ₂ S	✓*	✓
	Sulfur Hexafluoride	SF ₆		✓

* Volcanic/industrial/biomass burning plume column densities only

Measurement Requirements and Approaches

Introduction

The science requirements outlined above lead directly to a set of instrument and measurement requirements, shown in Table III. The detailed basis and justification for these requirements is far too long to reproduce here so only a brief outline follows. Ref. 2 is to a web site where further details may be found.

Spectral Properties. The species to be observed have their transitions widely scattered throughout the infrared, so an initial requirement is for broad spectral coverage (650 - 3050 cm^{-1}). Secondly, we want the spectral resolution to match the widths of the spectral features. Near the surface, weak Lorentz-broadened lines have a width $\sim 0.1 \text{ cm}^{-1}$, falling to $\sim 0.025 \text{ cm}^{-1}$ in the upper troposphere. Note that, within a factor of about 2, these widths are independent of species and frequency so we have chosen those values for the nadir and limb modes respectively. In turn, this requires a maximum optical path difference of 8.45 cm in the nadir and 33.8 cm at the limb. For a number of reasons, it is preferable that zero path difference (ZPD) be in the middle of the travel so these values are bi-directional.

Spectrometer Type. The foregoing lead inevitably to a Fourier Transform spectrometer (FTS)³ because: a) dispersive spectrometers do not have constant (frequency) resolution; b) gas correlation spectrometers are limited in the species they can observe and cannot cope with Doppler shifts and c) other technologies offer only restricted spectral coverage. We have chosen the Connes'-type 4-port configuration⁴ because (as discussed below) it permits us to optimize detector technologies by using 4 relatively-limited spectral regions which are further subdivided into 200 - 300 cm^{-1} bands through the use of interchangeable filters for background control and data-rate reduction.

Detector Arrays. One of the features of an FTS is that it readily supports an imaging mode which, in turn, improves collection efficiency over the more traditional spatially-scanning systems. We have chosen to employ 1x16 linear arrays whose size in one dimension was chosen to provide an individual pixel size of 2.3 km vertically at the limb and, in the other direction, 23 km parallel to the limb. Since the same arrays are also used in nadir, these number translate to 0.5 km in-track and 5 km cross-track. Furthermore, since an FTS is very susceptible to non-linearities, we wished to avoid using photoconductors; thus all 4 arrays are photovoltaic Mercury Cadmium Telluride (MCT).

Signal-to-Noise Ratio. As a rough rule-of-thumb, when the spectral signal-to-noise ratio falls below 30:1 it becomes very difficult to extract useful information from the data. Thus we have, somewhat arbitrarily, chosen 30:1 as our lower limit. With a 5 cm diameter beam and a scan time of 4 seconds (nadir) or 16 seconds (limb), we find (using a radiometric model) that at frequencies below about 2500 cm^{-1} we should be able to meet or exceed this goal under most conditions. At higher frequencies, some pixel and/or scan averaging will usually be necessary at nadir (even under sunlit conditions) and limb sounding becomes impracticable.

At the other extreme, the upper bound to signal-to-noise ratio is limited to about 600:1 by the 16-bit analog-to-digital converter (the best that can currently be obtained as a flight-qualified

component).

Pointing Accuracy. We use TES in a “staring” mode to avoid amplitude modulations due to scene variations (which can easily become the dominant noise source in an FTS). This, in turn, puts stringent requirements on the pointing accuracy. Unfortunately, using active feedback control from the scene (especially at the limb) is impracticable, so we must control the pointing mirror by “dead reckoning” using gyro attitude signals from the spacecraft. The most difficult direction is the pitch axis (the vertical direction at the limb) where a specification of 74 μ rad peak-to-peak is necessary due to the extreme radiance gradients (up to 40% per km) observed in the upper troposphere.

Field of Regard. The 2-axis pointing mirror not only must stabilize the line of sight but must also permit switching the field of view a) from nadir to the (trailing) limb, b) to cold space above the limb and c) to the internal calibration sources. This has the added benefit that TES is not limited to strictly nadir viewing - we can offset the downward view by up to 45° in any direction and either stare at a location (a volcano, for example) for over 3 minutes or, along the ground track, place the footprints contiguously to make transect observations covering more than 800 km. This mode is valuable for observing phenomena such as the regional ozone episodes that invade the eastern US in the summer.

Table III: TES Requirements & Specifications

Requirement	Value or Type	Comments
Spectrometer Type	Connes'-type 4-port Fourier Transform Spectrometer	Both limb & nadir viewing capability essential
Spectral Coverage	650 - 3050 cm^{-1} (3.2 - 15.4 μm)	Continuous, but with multiple sub-ranges typically 200 - 300 cm^{-1} wide (Table IV)
Spectral Resolution	Interchangeably 0.1 cm^{-1} downlooking or 0.025 cm^{-1} at the limb	Assuming Norton-Beer "medium" apodization
Optical Path Difference	Interchangeably ± 8.45 cm downlooking or ± 33.8 cm at the limb	Double-sided interferograms
Detector Spectral Coverage	1A: 1900 - 3050 cm^{-1} 1B: 820 - 1150 cm^{-1} 2A: 1100 - 1950 cm^{-1} 2B: 650 - 900 cm^{-1}	All MCT PV @ 65K. For the labeling convention, see Fig. 3.
Detector Array Configuration	1 x 16	All 4 arrays optically-conjugated
Beam Diameter	5 cm	Unit magnification system
System Étendue	$9.45 \times 10^{-5} \text{ cm}^2 \cdot \text{sr}$	Not allowing for a small central obscuration from the cassegrain secondaries
Modulation Index	> 0.7 ; 650 - 3050 cm^{-1}	> 0.5 at 1.06 μm (control laser)
Spectral Accuracy	$\pm 0.00025 \text{ cm}^{-1}$	After correction for finite field-of-view, off-axis effects, Doppler shifts, etc.
Channeling	$< 10\%$ peak-to-peak; $< 1\%$ after calibration	All planar transmissive elements wedged
Spatial Resolution	0.5 x 5 km nadir; 2.3 x 23 km limb	See Fig. 4
Spatial Coverage	5.3 x 8.5 km nadir; 37 x 23 km limb	See Fig. 4

Pointing Accuracy	75 μ rad pitch 750 μ rad yaw 1100 μ rad roll	Peak-to-peak values
Field of Regard	45° cone about nadir; plus trailing limb	Also views internal calibration sources
Scan (Integration) Time	4 sec nadir & calibration; 16 sec limb	Constant-speed scan, 4.2 cm/sec (OPD rate)
Maximum Stare Time, nadir	208 seconds	40 downlooking scans
Transect Coverage	885 km max	See Fig. 5
Interferogram Dynamic Range	≤ 16 bits	Plus 4 switchable gain steps
Radiometric Accuracy	$\leq 1\%$ 650 - 2500 cm^{-1} ; $\leq 2\%$ 2500 - 3050 cm^{-1}	Internal, adjustable, hot black body + cold space
Pixel-to-Pixel Cross Talk	$<10\%$	Includes diffraction, aberrations, carrier diffusion, etc.
Spectral Signal-to-Noise Ratio	Up to 600:1. 30:1 minimum requirement	Depends on spectral region & target. General goal is to be source photon shot noise limited
Lifetime	5 years on orbit	plus 2 years before launch
Size, Stowed	1.0 x 1.3 x 1.4 m	During launch
Size, Deployed	1.0 x 1.3 x 3.0 m	On orbit
Mass	385 kg	Allocation
Power, Average	334 W	Allocation
Power, Peak	361 W	Allocation
Data Rate, Average	4.5 Mbps	Science only
Data Rate, Peak	6.2 Mbps	Allocation

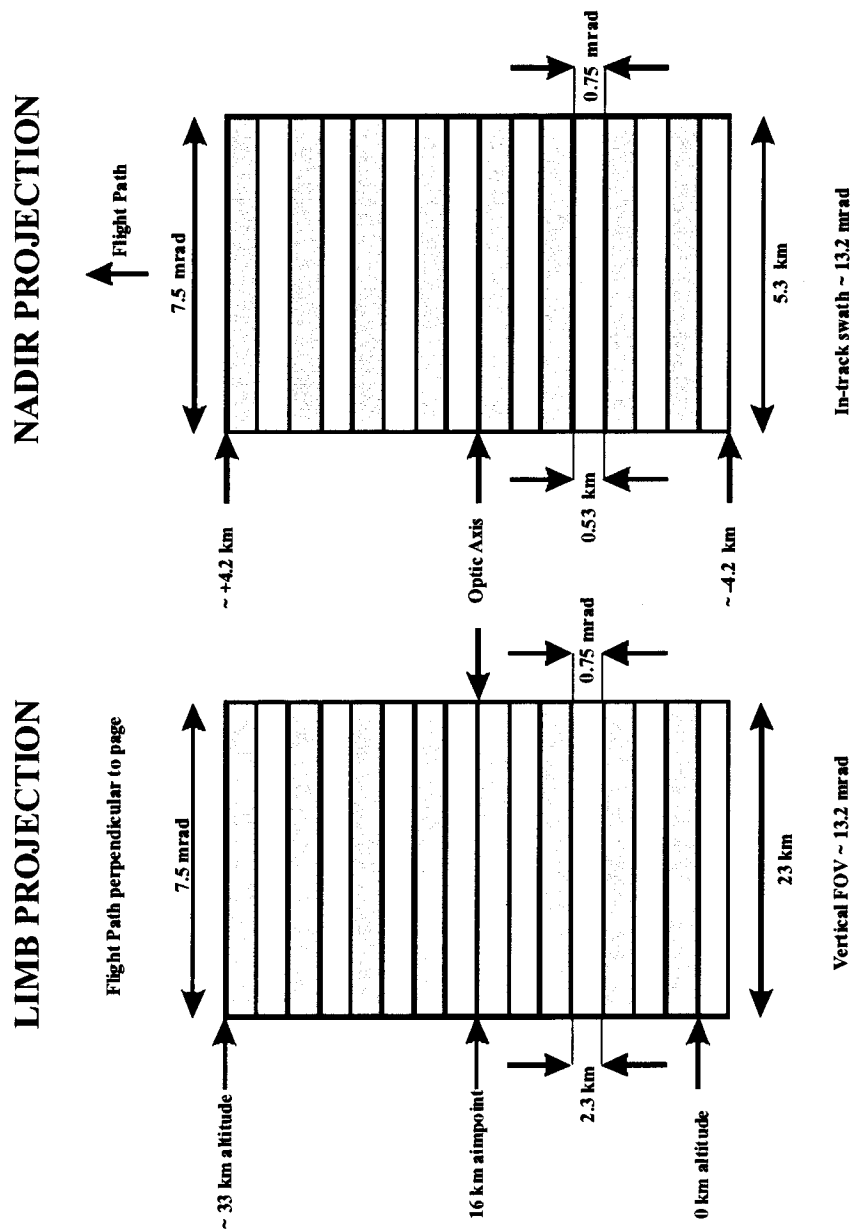


Fig. 8. TES detectors projected to the nadir and to the limb

Instrument Overview

Optical Layout

As indicated in Table III, TES is an imaging Fourier Transform Spectrometer to be used for the passive remote sensing of tropospheric chemistry in the mid- and far-infrared. Fig. 3 shows a schematic of the optical path.

The interferometer itself is a folded Connes'-type 4-port arrangement⁴. The key features are the use of:

i) Back-to-back cube corner reflectors on a common translator mechanism to provide the change in optical path difference. Zero path difference (ZPD) is in the middle of the travel so that double-sided interferograms can be recorded;

(Some hardware pictures may be added here)

ii) KBr for the beamsplitter/recombiner and the compensator. While KBr has many desirable properties such as good infrared transmittance and a low refractive index, it has numerous less-desirable ones such as low strength and resistance to deformation and is, of course, hygroscopic. While these certainly complicate handling and mounting, KBr has been used in space successfully in other instruments (e.g., ATMOS)⁵;

iii) Only one of the two input ports for actual atmospheric measurements. The other input views a grooved cold reference target. In principle, cold space could be used for the same purpose but the actual interferometer is deeply embedded in the structure (for thermal control reasons) and the provision of such a view would be quite complicated;

iv) A diode-pumped solid-state Nd:YAG laser for interferogram sampling control. Although the wavelength of the laser is rather longer than is really desirable (1.06 μm rather than the more common 0.63 μm of a HeNe laser), the lower voltages and power dissipation of the Nd:YAG make it, in our view, a better choice despite the need for temperature control of the laser head;

v) Cassegrain telescopes for condensing and collimating wherever possible in order to minimize the number of transmissive elements in the system;

vi) A passive space-viewing radiator (see below) to maintain the interferometer and most of the associated optics at 180 K. This reduces the thermal background noise and improves contrast because the tropopause region of the atmosphere can reach similar temperatures;

vii) A fold mirror and a 2-axis pointing mirror operating at ambient temperature (nominally 290 K, all other components except the calibration sources are cooled). Pointing is performed by "dead reckoning": the gimbal axes have 21-bit shaft encoders attached and, using these and spacecraft ephemeris and attitude information, the on-board computer calculates the necessary pointing

angles. Note that TES is inherently a staring sensor because any signal amplitude modulation (such as would be induced by pushbroom or whiskbroom scanning) is indistinguishable from the required interferometric modulation;

viii) Two independent focal plane assemblies maintained at 65 K with active pulse-tube coolers. The assemblies accept the dual outputs of the interferometer (labeled "1" & "2"), which are further split by dichroics into "A" and "B" channels, whence the designations in Table III. Thus there are 4 independent focal planes, each an array of 1×16 elements, and optically conjugated so that equivalent pixels in each focal plane see the same target. Each focal plane is photovoltaic MCT optimized for a different spectral range (see Table III). In addition, each has an independent filter wheel in which the filters are typically $200 - 300 \text{ cm}^{-1}$ wide (Table IV). This not only reduces instrument background control but permits undersampling of the interferograms (the sampling interval is between 8 and 11 laser fringes per sample) and a consequent reduction in data rate and volume (i.e., provides a form of lossless data compression).

Signal Chains

Each of the 16 pixels in each array has an independent signal chain (i.e., 64 in all). The implementation uses Application-Specific Integrated Circuits (ASIC's) with 4 levels of switchable gain and switchable electronic bandpass filters (designed to match the optical bandpasses) for noise control. Output is provided by 16-bit analog-to-digital converters triggered by the Nd:YAG laser sub-system. The digital outputs are multiplexed into a single packetized serial bit stream and transmitted to the spacecraft *via* a TAXI interface. The output science data rate averages 4.5 Mbps.

(May need more?)

Thermal and Mechanical

Insofar as possible, TES is constructed from graphite-fiber composites (the reflecting optical elements being gold-coated beryllium). The whole is a box $1.0 \times 1.3 \times 1.4 \text{ m}$ when stowed, expanding to $1.0 \times 1.3 \times 3.0 \text{ m}$ when the Earth shade for the 180 K radiator is extended on orbit (Fig. 1). Most of the exterior surfaces are used as radiators for the various sub-assemblies - the problem one has in space is not one of providing sufficient input power but of dissipating the waste heat. A particular feature of the thermal design is the use of loop heat pipes to transfer this waste heat from its sources (electronic components, for example) to the radiators. Loop heat pipes, a relatively new technology, have the virtue that they operate both in a 1g environment and in space (unlike conventional heat pipes).

In order to control the thermal environment both before and after launch (and for 5 years thereafter), the system has heaters to maintain a constant interior temperature. Although modern graphite composites have a low coefficient of thermal expansion (comparable to Invar), interferometers have a low tolerance for differential expansions, so such control is essential.

Table IV: FILTER BANDS & SPECIES COVERAGE

Filter ID	Filter Half-Power Points, cm ⁻¹		Temperatures	Major Species
Array 2B (650 - 900 cm ⁻¹)				
2B1	650	900	T _a	CO ₂ , HNO ₃ , CFC11, NO ₂
Array 1B (820 - 1150 cm ⁻¹)				
1B1	820	1050	T _b	HNO ₃ , NH ₃ , CFC11, CFC12, O ₃
1B2	950	1150	T _b	O ₃ , NH ₃ , CFC11, CFC12, N ₂ O
Array 2A (1100 - 1950 cm ⁻¹)				
2A1	1100	1325	T _b	O ₃ , N ₂ O, HNO ₃ , CFC12, SO ₂ , CH ₄
2A2	1300	1550		O ₃ , HNO ₃ , CH ₄
2A3	1500	1750		H ₂ O, NO ₂
2A4	1700	1950		H ₂ O, NO
Array 1A (1900 - 3050 cm ⁻¹)				
1A1	1900	2250	T _a	T _b O ₃ , CO, N ₂ O, NO, OCS
1A2	2200	2450		CO ₂ , N ₂
1A3	2425	2650		T _b N ₂ O
1A4	2600	2850		T _b HDO
1A5	2800	3050		T _b CH ₄ , HCl, O ₃

Notes: T_a = Atmospheric Temperature Profile; T_b = Surface Temperature & emissivity

In-Flight Calibration

An emission-mode sensor such as TES is critically dependent on its radiometric calibration if valid retrievals are to be made from its spectra. Accordingly, TES has an internal full-aperture cavity black body source to which the pointing mirror can be directed. The temperature of this black body is adjustable between ambient (~ 290 K) and 340 K. Most routine calibrations are performed at 340 K for the hot point and cold space for the baseline (offset). However, although PV detectors are much less susceptible to non-linearity than PC detectors, the potential for non-linearity elsewhere in the signal chain always exists so, from time-to-time, the internal source will be varied in temperature over its entire range so the effect (if any) can be monitored.

Most standard calibrations will be obtained at 0.1 cm^{-1} resolution and FFT-interpolated for the limb scans at 0.025 cm^{-1} resolution. This presupposes that there are no sources of sharp-line spectral features internal to TES. Occasionally, therefore, we will acquire calibration data at the higher resolution to check this hypothesis.

TES also has an on-board spatial calibrator (an illuminated slit) that the pointing mirror will sweep over the detector arrays to check the co-alignment of the arrays.

Contamination

TES is a cryogenic instrument and, as such, is very susceptible to contamination from outgassing not only internally but also from the rest of the spacecraft. Most vulnerable, of course, are the focal planes (the coldest points in the system). We will monitor this through the calibration signals - when these fall by 5%, decontamination heaters will be turned on to raise the entire instrument to about 10 C in order to drive off any condensates (expected to be water vapor, carbon dioxide and residual hydrocarbons in the main).

Operational Modes

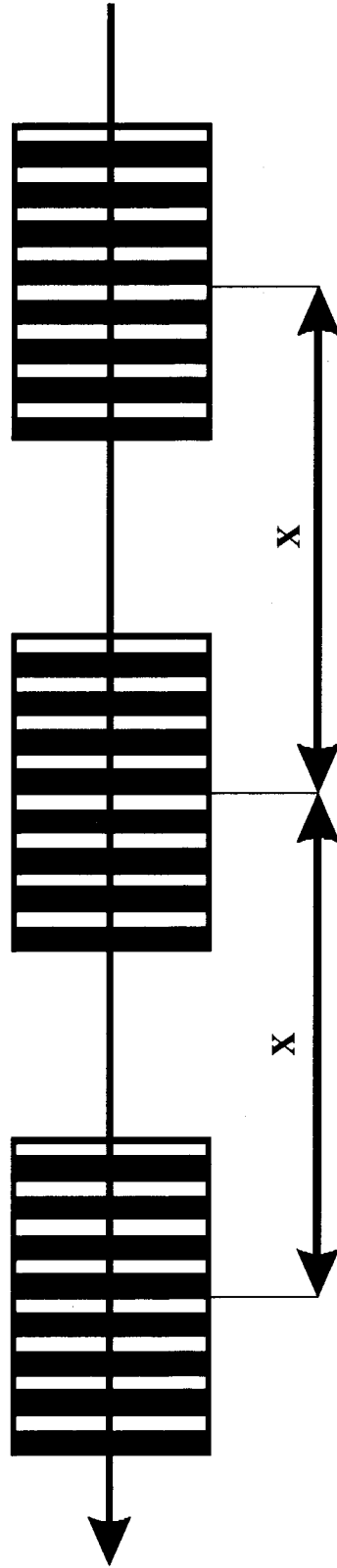
Introduction

As indicated earlier, TES inherently operates in a step-and-stare mode when downlooking. At the limb, of course, the footprint is smeared along the line of sight by about 110 km during a 16 second limb scan (comparable to the effective size of the footprint itself). Thus horizontal inhomogeneity in the atmosphere becomes an issue that must be dealt with in data processing (usually through a simplified form of tomography). Furthermore, the long path through the limb makes cloud interference almost inevitable; rarely does a limb view penetrate to the boundary layer. Nevertheless, the benefits of limb viewing for trace gas analysis in the mid and upper troposphere are so great as to outweigh any disadvantages.

Global Surveys

The routine operating mode for TES is to make continuous sets of nadir and limb observations (plus calibrations) on a 4-day-on, 4-day-off cycle (58 orbits each). During the “off” days, TES is not actually powered down. These are the times for making extensive calibrations and for the Special Product modes (see below). The main argument for such discontinuous sequencing is the sheer volume of data generated in 4 days (about 650 Gb). This stresses not only the data analysis process but, more importantly, the ability of the scientific community to assimilate the information.

An overview of the acquisition process is shown in the upper part of Fig.6. The lower part shows how this is broken up into 81.2 second sequences of calibration, nadir and limb observations. The timing is based on the need for the sampling density to be commensurate with the roughly 5° latitude grid of current chemical/dynamical atmospheric models. Furthermore, acquisition is triggered by the crossing of the southernmost point in the orbit (the southern apex). Thus observations are made at the same latitudes on every orbit and, every 16 days, identical locations sampled (Fig. 7).



STEP-and-STARE $\left\{ \begin{array}{l} 0 < X < 1490 \text{ km} \\ \text{for } 5 < t < 221 \text{ sec} \end{array} \right.$

TRANSECT:

Footprints are exactly contiguous in a line up to 885 km long

Fig. 5: TES Step-and-Stare and Transect Mode

NADIR & LIMB GLOBAL SURVEY STRATEGY

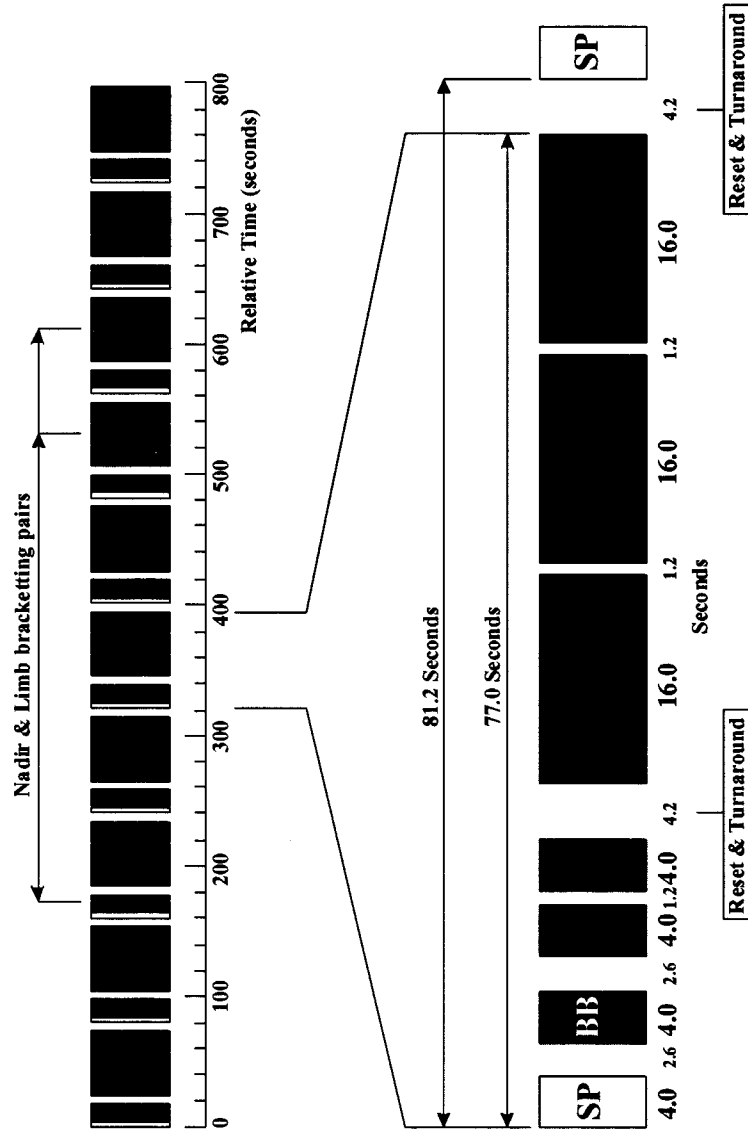


Fig. 6: Phasing of Limb and Nadir observations in Global Surveys

Intensive Campaigns

Intensive Campaigns fall under the "Special Product" rubric and are necessarily conducted in-track. There are two types presently envisaged: downlooking transects and continuous limb observations. Transects involve pointing forwards 45° and staring for one or more 4 second scans. The footprint is then stepped backwards so that the new footprint is contiguous to the previous one (Fig. 5). Of course, the spacecraft is moving forward during this time at about 7 km/s so eventually the transect passes through nadir and is terminated when the nadir angle is 45° backwards. The 45° limit is somewhat arbitrary but is roughly the condition beyond which line-of-sight inhomogeneity and refraction would complicate the analysis. Furthermore, the footprint stretches as one goes off-nadir with a consequent loss of spatial resolution. Transects can be up to 885 km long and will typically be used to study regional ozone episodes such as occur over the Eastern US in summer. Limb campaigns are unlimited in length and will usually be used to investigate upper troposphere impacts of large volcanos (exemplified by the Mt. Pinatubo eruption in 1991) and tropical biomass burning in September/October. Similar campaigns will be undertaken for intercomparisons with the other CHEMISTRY 1 instruments and in validation programs.

Special Events

Special Events use the ability of TES to point at specific locations for a few minutes on any given orbit. Notable among these targets are gas-emitting volcanos (e.g., Kilauea in Hawaii) whose gas admixtures are believed to be eruption predictors. Since TES can point anywhere within 45° of nadir (cross-track and in-track) almost everywhere on Earth can be reached some time during a 16 day interval.

Data Analysis

TES data processing falls naturally into 4 groups (the “Level” terminology is NASA’s):

- 1) *At Level 1A*, the raw data from the spacecraft are decommutated and the interferograms reconstructed. File headers also contain important ancillary data such as time, date, spacecraft and target location, and instrument pointing angle.
- 2) *At Level 1B*, the interferograms are phase-corrected and converted to spectra, radiometrically-calibrated and resampled onto a common frequency grid. Certain data quality flags are added to the header at this juncture and the results passed to Level 2⁶.
- 3) *At Level 2*, vertical concentration profiles of the selected species are retrieved from the spectra⁷.

Briefly, all modern retrieval algorithms are somewhat alike: based on an initial estimate of the physical/chemical state of the atmosphere at the time and location of the observation (the so-called *first guess*), the appropriate version of the Equation of Radiative Transfer is solved to provide an estimate of the expected spectral radiance as seen by the instrument. This *forward model* is compared to the observed spectral radiance and the parameters of the atmospheric state adjusted (using specified rules) to bring the forward model into closer agreement with the observation. The process is iterated until, by other specified rules, convergence is achieved. The resulting *state vector* of atmospheric parameters is the desired result. Most algorithms also provide an objective estimate of the accuracy of the retrieval.

- 4) *At Level 3*, the profiles are resampled onto appropriate surfaces (usually pressure) to provide a series of maps (one set for each species). This, we believe, will be the most commonly-accessed TES browse product although serious users will then most likely request the Level 2 profiles themselves. Note that it is EOS data policy that all products are in the public domain and available from the archives at the marginal cost of reproduction. TES data will be archived and available from at the NASA Langley Research Center Distributed Active Archive Center (DAAC) in Hampton, VA.

Conclusions

Although uncommon in this type of paper, we have felt it to be important that the reader be able to follow the reasons why specific instrument parameters and characteristics were chosen, flowing from the overall mission requirements down to the specific hardware implementation. In many cases, there were equally good or bad alternatives but over-riding requirements for any space experiment are cost and schedule. Reliability through redundancy is also preferred but cost considerations have dictated that TES be largely a single-string instrument with little or no duplication of parts.

In a subsequent paper we shall discuss the measured characteristics of TES as compared to the pre-flight performance models on which much of the design is based. However, we have high confidence that the goals will be met because TES shares many of the characteristics of an airborne precursor called the Airborne Emission Spectrometer (AES). AES has flown many times on a variety of aircraft (a severe environment for any instrument) with good success⁸ and has proven to be an invaluable test-bed both for hardware and for data analysis.

We should be remiss were we not to express our sincere thanks to the many individuals who have contributed to this program. The full list would run to well over 100 names but we do especially wish to thank Robert J. McNeal of NASA HQ for his long-standing support, Daniel Jacob and Jennifer Logan of Harvard University for keeping us focused on our primary objective, Tony Clough of AER Inc. and Clive Rodgers of Oxford University for their keen analytical insights, and Ed Miller and Helen Worden of JPL without whom this instrument could never be built.

The research reported in this paper was conducted by the Jet Propulsion Laboratory, California Institute of Technology, under a contract with the National Aeronautics and Space Administration.

References

1. *Earth Science Strategic Enterprise Plan 1998-2002*, NASA HQ, Washington D.C. October 1998 (<http://www.earth.nasa.gov/visions/stratplan/index.html>)
2. Tropospheric Emission Spectrometer Scientific Objectives & Approach, Goals & Requirements, Version 6.0. JPL D-11294, April 1999 (<http://www.>)
3. Beer, R. *Remote Sensing by Fourier Transform Spectrometry*. Wiley & Sons, NY (1992)
4. Connes, J. and P. Connes, Near-infrared planetary spectra by Fourier spectroscopy. I: Instruments and results, *J. Opt. Soc. Am.*, **56**, 896-910 (1966)
5. Farmer, C.B. "High resolution infrared spectroscopy of the Sun and the Earth's atmosphere from space", *Mikrochim. Acta (Wien)*, **III**, 189-214 (1987)
6. Level 1B Algorithm Theoretical Basis Document JPL D-16479, Jan 1999 (<http://www.>)
7. Level 2 Algorithm Theoretical Basis Document JPL D-16474, Jan 1999 (<http://www.>)
8. Worden, H.M., R. Beer and C.P. Rinsland, Airborne infrared spectroscopy of 1994 western wildfires. *J. Geophys. Res.* **102**, 1287-1299 (1997)